AN ABSTRACT OF THE DISSERTATION OF

Alex C. Misner for the degree of Doctor of Philosophy in Nuclear Engineering presented on April 25, 2008.
Title: Simulated Antineutrino Signatures of Nuclear Reactors for Nonproliferation Applications.

Abstract approved:

Todd S. Palmer

Antineutrino detectors could provide a valuable addition to current safeguards regimes. Antineutrinos are an attractive emission to monitor due to their low interaction cross-section that prevents them from being shielded and the dependence of their spectrum on the power level and isotopic content of a reactor core. While there are antineutrino detectors currently deployed at an operational reactor, such observations cannot predict the effect of the diversion of nuclear material on the antineutrino emissions. Utilizing simulation tools, one can predict the antineutrino signatures of such abnormal operations and other reactor types that have not been experimentally measured. This study simulates reactor cores with assembly-level resolution for both baseline and diversion cases in order to predict the properties of a detector for measuring the differences in the antineutrino signatures.

Simulated Antineutrino Signatures of Nuclear Reactors for Nonproliferation Applications

by
Alex C. Misner

A DISSERTATION

submitted to

Oregon State University

in partial fulfillment of
the requirements for the
degree of

Doctor of Philosophy

Presented April 25, 2008
Commencement June 2008

Doctor of Philosophy dissertation of Alex C. Misner presented on April 25, 2008.

APPROVED:

Major Professor, representing Nuclear Engineering

Head of the Department of Nuclear Engineering and Radiation Health Physics

Dean of the Graduate School

I understand that my dissertation will become part of the permanent collection of Oregon State University libraries. My signature below authorizes release of my dissertation to any reader upon request.

Alex C. Misner, Author

ACKNOWLEDGEMENTS

I would like to thank my advisor, Dr. Todd Palmer for the guidance and encouragement he provided over the course of my graduate career. His insights have proved invaluable in developing my skills as a researcher.

I also would like to thank my collaborators at Lawrence Livermore National Laboratory, Drs. Adam Bernstein, Nathaniel Bowden, and Robert Svoboda. Mrs. Nancy Hutcheon of the Seaborg Institute at LLNL provided invaluable help in obtaining a fellowship that partially funded my research.

I would like to thank Drs. Steve Binney and Kathryn Higley for helping to coordinate the INIE-sponsored course at LLNL that lead to my involvement with this project.

Finally, I would like to thank my family and friends for all of the support and encouragement throughout my student career.

TABLE OF CONTENTS

Page

LIST OF FIGURES

LIST OF FIGURES (CONT'D)

LIST OF TABLES

LIST OF ACRONYMS

BOC	Beginning of Cycle
EAF	European Activation File
ENDF	Evaluated Nuclear Data File
EOC	End of Cycle
FENDL	Fusion Evaluated Nuclear Data Library
FSAR	Final Safety Analysis Report
GNEP	Global Nuclear Energy Partnership
IAEA	International Atomic Energy Agency
LANL	Los Alamos National Laboratory
LEU	Low-Enriched Uranium
LLNL	Lawrence Livermore National Laboratory
MAP	Modified Additional Protocol
MASLWR	Multi-Application Small Light Water Reactor
MOC	Middle of Cycle
MOX	Mixed Oxide
NPT	Nonproliferation Treaty
ORIGEN-ARP	Oak Ridge Isotope Generation - Automated Rapid Processing
PARCS	Purdue Advanced Reactor Core Simulator
PWR	Pressurized Water Reactor
SNL	Sandia National Laboratory
SONGS	San Onofre Nuclear Generating Station
SQP	Small Quantities Protocol

Simulated Antineutrino Signatures of Nuclear Reactors for Nonproliferation Applications

1. Introduction

The proliferation of nuclear weapons is one of the key issues in global security today. Safeguards regimes are put into place in an attempt to prevent the diversion of nuclear material from power reactors to weapons programs. Currently, safeguards are largely based on operators' logbooks and verification of the content of spent fuel pools. Antineutrinos provide a potential method of verifying the operating conditions and isotopic content of a nuclear reactor without disrupting operations. Antineutrinos offer advantages over other forms of radiation because they are almost impossible to shield. The same penetrating property that gives antineutrinos this advantage, however, makes them very difficult to detect compared to other forms of radiation.

While it is possible to experimentally measure the antineutrino spectrum of an operating reactor, these measurements only give information about the normal operations of the power plant. This presents the problem of how to determine if a detector is suitable for monitoring for the illicit removal of fissile material from the reactor. Because it is not generally feasible to have a reactor facility actually operate in a manner that would resemble proliferation activities, the only practical way to evaluate detection technologies is to predict the effect of these activities on the antineutrino spectrum through computer simulation.

In addition to examining reactors fueled with low-enriched uranium (LEU), this study will investigate the antineutrino signature of reactors that utilize mixed-oxide (MOX) fuel. A MOX-fueled reactor contains much higher levels of plutonium than an LEU-fueled reactor, and as such may present an attractive proliferation target. This study will also investigate the use of antineutrino detectors for the Multi-Application Small Light Water Reactor (MASLWR). MASLWR is a new reactor design being developed at Oregon State University as a part of the Global Nuclear Energy Partnership (GNEP) program. Antineutrino detection could be a desirable method to measure the power of MASLWR because of the design of its cooling system. MASLWR utilizes natural circulation to move its cooling water rather than pumps. This means that is critical to minimize the obstruction of the flow paths of this coolant. An antineutrino detector could provide a method of determining the reactor power level without introducing any extra equipment inside of the reactor vessel that would produce such an obstruction. A description of the core design will be given in chapter 2.

The specific questions this study aims to answer are as follows: Is ORIGEN-ARP a tool capable of accurately predicting the antineutrino emissions of an operating reactor? Through which methods would it be possible to detect abnormal operating conditions of a reactor that could be signs of material diversion? What is the difference in the antineutrino signatures of reactors fueled with LEU and MOX? What, if any, modifications would have to be made to an antineutrino detector for it to be used as a power monitoring device on MASLWR? What properties would a detector have to possess to sense an abnormal operating condition?

The remainder of this chapter will provide the background to this study. The history of safeguards regimes will be described as will the physics of fuel depletion. This chapter will cover the basics of the physics of antineutrino detection and neutrino oscillation. A description of the technology of antineutrino detectors currently in use and development will also be included. The history of reactor antineutrino experiments will be given in order to provide a context within which the results of this study could be applied. Finally, a description of the simulation package ORIGEN-ARP will be given.

1.1 History of Nuclear Safeguards

Nuclear safeguards can be traced back to the Atoms for Peace speech. (Eisenhower 1953) In that address, President Eisenhower laid out a vision of the peaceful use of nuclear technology in the world. The creation of the International Atomic Energy Agency (IAEA) was a key provision set forth in the speech. As envisioned by the president, the IAEA would be a repository for uranium and other fissionable material, which would then be distributed to countries around the world for peaceful applications. The scientific staff of the proposed IAEA were specifically tasked to devise methods to ensure that the nuclear material be used only for these approved activities rather than military purposes.

The IAEA was later established by statute at the United Nations. (IAEA 1957) The first international safeguards framework was enumerated in article XII of that document. This article states that the agency shall create a staff of inspectors to enact these safeguards. The specific methods listed in the article include the approval of the design of equipment and facilities, the verification of operating records, and the oversight of processes that involve the separation of radioactive material. In the event of noncompliance, the document states that violators must take any requested corrective measures in a reasonable period of time.

The next document to significantly impact safeguards was the Treaty on the Non-Proliferation of Nuclear Weapons or the Non-Proliferation Treaty (NPT). (IAEA 1970) This treaty prohibits the transfer of nuclear weapons technology to non-nuclear-weapons states. In the context of the NPT, the nuclear-weapons states are the United States, the United Kingdom, France, the Soviet Union (now Russia), and the People's Republic of China. In addition to not accepting the transfer of technology, non-nuclear-weapons states are bound to not develop nuclear weapons programs of their own. Safeguards are specifically addressed in article III of the treaty. Non-nuclear-weapons states are obligated to enter into an agreement with the IAEA to accept the oversight described in the founding statute of that organization. These safeguards are to be applied to any facility that possesses fissionable material that is under the jurisdiction of the member state. No specific remedies to noncompliance are listed in the NPT.

In the IAEA's agreement with Ecuador, the Small Quantities Protocol (SQP) was created. (IAEA 1974) This protocol allowed states to possess nuclear material in amounts lower than certain limits without the implementation of comprehensive safeguards provisions. In 2005, this protocol was modified to require initial reports on the amount of nuclear material present and to only apply to states without planned or existing nuclear facilities.

In the late 1990's, the Model Additional Protocol (MAP) was developed to increase the effectiveness of safeguards regimes. (IAEA 1997) The MAP must be adopted by each state individually and coexists with the earlier safeguards agreement between that state and the IAEA. When the MAP and the original agreement are in conflict, the provisions of the MAP apply. The MAP expands previous safeguards regimes by requiring an account of all nuclear-fuel-cycle-related research that does not directly involve nuclear material. It also requires a description of each building at a nuclear site rather than just a site description. Information regarding the location, operational status, and production capability of uranium mines and enrichment facilities for uranium and thorium must be provided to the IAEA under this agreement. The MAP also requires an account of the quantity, chemical composition, and intended use for nuclear material that is not of sufficient grade to be used as nuclear fuel. States are responsible for the reporting of any high level waste containing plutonium, highly-enriched uranium, or ^{233}U under this protocol. Besides the detailed responsibilities of member states listed in the MAP, it also provides a detailed framework for inspectors to gain access to facilities. Under this agreement, inspectors shall be granted access to nuclear facilities to verify the following conditions: the absence of banned material and the accuracy of reports given to the IAEA. While access must be given to the inspectors, the inspectors must provide written notice describing the reason for and the activities to be carried out during the inspection in advance of their arrival (usually 24 hours).

The founding statute of the IAEA along with the SQP and the MAP form the basis of the safeguards regimes currently in use.

1.2 Fuel Depletion

Fuel depletion is the process of the fissile isotopes in nuclear fuel being consumed in fission reactions. (Duderstadt and Hamilton 1976) The fissions in nuclear reactors are caused by the absorption of neutrons by the nuclei present in the fuel. In addition to inducing fissions, neutron absorption can cause the transmutation of nuclei into other elements. Of particular interest is the creation of plutonium through this process. This occurs through the reaction shown below.

$$U^{238} + n \rightarrow U^{239} + \gamma \rightarrow Np^{239} + \beta^- + \bar{\nu} \rightarrow Pu^{239} + \beta^- + \bar{\nu}$$

This reaction transforms a non-fissile isotope into a fissile nuclide that is desirable for use in nuclear weapons. The ^{239}Pu can also absorb two more neutrons to become ^{241}Pu, another fissile isotope.

Depletion analysis is important to any reactor model in order to ensure that the fuel can sustain the chain reaction that powers it as well as still be effectively controlled by safety systems. In addition to the concerns during the operation of a reactor, depletion analysis is critical for the characterization of spent fuel. In the case of spent fuel, there is a safety concern in addition to the nonproliferation and criticality concerns that are present in reactor scenarios. The fission products that are inevitably produced when fuel is exposed to a neutron flux are often radioactive themselves, so it is necessary to know what the emissions of the spent fuel are so that they can be properly shielded.

The depletion of fuel is also important for nonproliferation applications. As the fuel is depleted, the plutonium content changes. Because isotopes of plutonium are attractive for weapons purposes, knowledge of the amounts of these isotopes present in the fuel can provide insight into proliferation risks.

In order to perform a depletion analysis, one must solve a series of coupled differential equations known as the Bateman equations. These are described in more detail in section 1.8.

1.3 Physics of Antineutrino Detection

Unlike more familiar particles, such as protons, neutrons, and electrons, antineutrinos are extremely difficult to detect. Pauli first postulated the existence of neutrinos in 1930 (unpublished) as a way of explaining why β particles are emitted from nuclei with a continuous spectrum. Fermi later built on this postulate in his theory of β-decay (Fermi 1934). However, at the time no direct evidence of the new particle existed. The difficulty in detecting antineutrinos arises from the fact that they are uncharged, nearly massless leptons, and therefore are not affected by either the electromagnetic or the strong nuclear force. The only force that significantly affects antineutrinos is the weak nuclear force, which has a shorter range and is much weaker than the aforementioned forces.

Antineutrinos are released when a nucleus undergoes β-decay. In the case of nuclear reactors, these decays occur in the fission products and their daughters. On average, each fission event will result in the emission of six antineutrinos. Figure 1.1 illustrates the genesis of the antineutrinos from fission. The number and energy distribution of these antineutrinos depends on the isotope that undergoes fission. Figure 1.2 shows the energy spectra of fission antineutrinos.

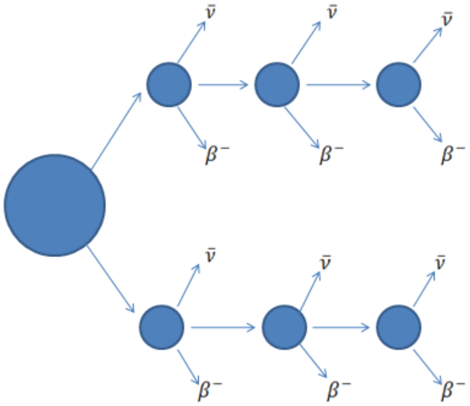

Figure 1.1: Antineutrinos from fission

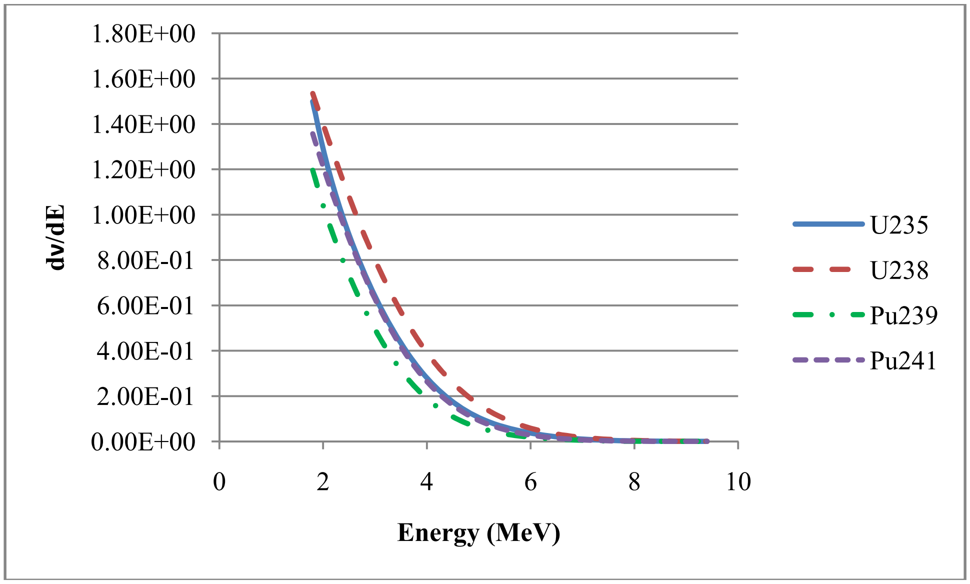

Figure 1.2: Antineutrino spectra from fission

From figure 1.2, it is clear that ^{238}U emits the most antineutrinos per fission and ^{239}Pu emits the least. However, there is only a very slight difference in the antineutrino emissions of the fission products of ^{235}U and ^{241}Pu.

The primary method used in the detection of antineutrinos is the inverse β-decay reaction on either a proton or a deuteron. The equations for these reactions are shown below.

$$\bar{\nu} + p \rightarrow \beta^{+} + n$$

$$\bar{\nu} + d \rightarrow \beta^{+} + n + n$$

In these reactions, the positron product deposits its kinetic energy and then annihilates with an electron, emitting γ-rays that are then detected. This process is rapid and produces what is referred to as the “prompt signal”. Product neutrons are then absorbed by an isotope that is added to the detection medium (dopant) which then decays one or more times, emitting γ-rays. This occurs on the order of tens of microseconds after the positron annihilation and is referred to as the “delayed signal”. (Bernstein, Wang, et al.

2002) Figure 1.3 illustrates these reactions as they occur in a detector. Antineutrino detectors look for these two events to happen in coincidence, which has the added benefit of reducing the background signal.

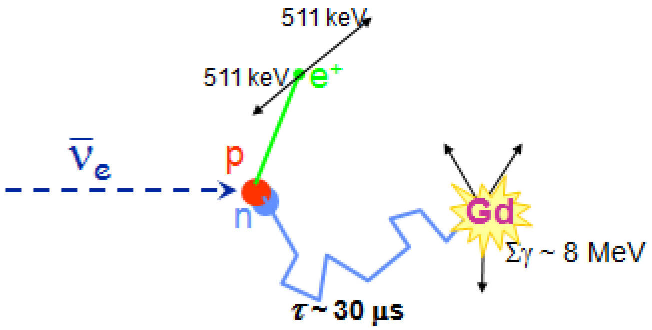

Figure 1.3: Inverse β-decay reaction in an antineutrino detector

An important background radiation source for antineutrino measurements is cosmic muons. Muons must be shielded because one of their decay products is an antineutrino. (Constant 1963) The decay scheme for a muon is shown below.

$$\mu^- \rightarrow \nu_\mu + \bar{\nu} + e^-$$

This background signal is reduced by the use of active shielding around the antineutrino detector. The active shielding in the earliest detectors consisted of Geiger-Müller tubes placed around the active volume of the detector. (Reines 1996) Currently, detectors that utilize an active shield use plastic scintillator panels.

Another source of false positive measurements is neutrons. A neutron can cause a proton to recoil in a scattering interaction, which will result in scintillation events. The neutron will then be absorbed by a gadolinium nucleus in the detection medium, creating a second scintillation event. The coincidence of these signals can be mistaken for the prompt and delayed signals of an antineutrino absorption.

1.4 Neutrino Oscillation

There are currently two areas of research involving the detection of reactor-generated antineutrinos: reactor safeguards and neutrino oscillations. While the application of the resulting data is different, the detectors may be used for either goal.

Antineutrinos, like other leptons, exist as a superposition of three mass eigenstates. These eigenstates correspond to the electron, the muon, and the tau. The state vector of a neutrino born into state *j* that has traveled distance L is given in equation 1.1.

$$|\nu_j\rangle = \sum_{\mathrm{k}} \left[\sum_{n} \mathrm{U}^*_{jn} \mathrm{e}^{-\mathrm{i}\left(\frac{\mathrm{m}_\mathrm{n}^2}{2\mathrm{E}}\right)\mathrm{L}} \mathrm{U}_{kn} \right] |\nu_k\rangle \tag{1.1}$$

where U is the lepton-mixing matrix. The value of U^*_{jn} is the probability of a weak interaction producing the lepton pair $l^+_j + \nu_n$. The values of the mixing matrix are given below. (Rodejohann 2004)

$$\begin{bmatrix} c_{12}c_{13} & s_{12}c_{13} & s_{13}e^{-i\delta} \\ -s_{12}c_{23} - c_{12}s_{23}s_{13}e^{i\delta} & c_{12}c_{23} - s_{12}s_{23}s_{13}e^{i\delta} & s_{23}c_{13} \\ s_{12}s_{23} - c_{12}c_{23}s_{13}e^{i\delta} & -c_{12}s_{23} - s_{12}c_{23}s_{13}e^{i\delta} & c_{23}c_{13} \end{bmatrix} \begin{bmatrix} \mathrm{e}^{\mathrm{i}\alpha_1/2} & 0 & 0 \\ 0 & \mathrm{e}^{\mathrm{i}\alpha_2/2} & 0 \\ 0 & 0 & 1 \end{bmatrix}$$

In the above matrix, c_{ij} is $\cos\theta_{ij}$ and s_{ij} is $\sin\theta_{ij}$, where θ_{ij} is a mixing angle. δ, α_1, and α_2 are CP-violating phases. The mixing angles are related to the probability of a flavor change by the expression shown in equation 1.2.

$$P(\nu_i \rightarrow \nu_j) = \sin^2(2\theta_{\mathrm{ij}})\sin^2\left(\frac{\Delta \mathrm{m}^2 \mathrm{L}}{4\mathrm{E}}\right) \tag{1.2}$$

The quantity $\sin^2(2\theta_{ij})$ is what experiments actually solve for when they state they are solving for θ_{ij}.

1.5 Types of Antineutrino Detectors

There are a number of designs that either have been used or have been proposed for detecting antineutrinos. The oldest and most common is a liquid scintillator. This was first proposed for antineutrino research in the early 1950s (Cowan, et al. 1953). Other detector designs include solid state and plastic scintillators.

A Cherenkov detector is a design that is not based on scintillation. Cherenkov radiation is emitted when a charged particle moves through a dielectric medium at a velocity greater than the speed of light in that medium. The charged particles that create the Cherenkov radiation in an antineutrino detector are electrons that have been scattered by the antineutrinos (or neutrinos). (Fukuda, et al. 2003) Cherenkov detectors have the advantage of being insensitive to the proton scatter caused by a fast neutron entering the detector. This is due to the large mass of the proton preventing it from achieving a high enough velocity when scattered by a neutron for it to emit Cherenkov light. The Cherenkov detectors also have the advantage of using nonvolatile media, such as water, where as scintillators tend to use flammable liquids. However, when comparing a water-based Cherenkov detector to a mineral oil-based liquid scintillator, the proton density is lower. This means that antineutrinos are less likely to be absorbed in a Cherenkov detector than a liquid scintillator of equal size.

Lawrence Livermore National Laboratory (LLNL) is currently investigating an antineutrino detector that uses a different mechanism than inverse β-decay. This detector is designed to detect the coherent scattering of nuclei caused by neutrinos and antineutrinos (Bernstein, et al. 2007a). This type of scattering is a prediction of the standard model of particle physics that has yet to be observed. The University of

Chicago is also developing a germanium-based detector to observe this interaction (Barbeau, et al. 2007) These detectors work by measuring the slight recoils of nuclei impacted by antineutrinos.

1.6 Reactor Neutrino Experiments

There have been several previous experiments that have utilized nuclear reactors as a source for antineutrinos. The earliest of these was the experiment that first detected the antineutrino (Reines and Cowan 1953). In this experiment, a cadmium-laced liquid scintillator was used to detect the products of the inverse β-decay caused by the absorption of an antineutrino by a proton. The reactor was located at the Savannah River facility. This work was later refined by the addition of NaI crystals to capture the γ-rays emitted by the annihilation of the positron and the neutron capture (Nezrick and Reines 1966). This improved study also replaced the cadmium dopant with gadolinium.

Several important antineutrino studies have taken place in Russia. The Krasnoyarsk reactor has been used to determine the interaction cross-section of the antineutrino with both the proton and the deuteron (Kozlov, et al. 2000). An experiment utilizing a VVER reactor provided the first observational evidence that the burnup of fuel could be observed with the antineutrino count rate (Klimov, et al. 1994). In addition to these measurements, Russian experiments have provided a greater understanding of the spectral distribution of antineutrinos emitted by a reactor. This work will be described in a later section.

There is an ongoing effort to measure the neutrino mixing angle θ_{13} in France. The CHOOZ experiment utilized a five ton liquid scintillator detector placed 1 km from the reactor core (Apollonio, et al. 2003). The experiment ran for over a year and set an upper limit on θ_{13}. This work is being expanded upon by the Double CHOOZ experiment (Ardellier, et al. 2004). Double CHOOZ improves on the earlier work by utilizing two ten-ton detectors, one placed 100 meters from the core and the second placed in the same cavern used for the original CHOOZ experiment 1 km from the core. Double CHOOZ hopes to determine the value of θ_{13} to within 0.02. There is now a proposal to improve on Double CHOOZ with Triple CHOOZ (Huber, et al. 2006). This would add a 200 ton detector in a second cavern at roughly the same distance as the far detector five years after the start of the Double CHOOZ experiment. If this occurs, θ_{13} could be determined with an uncertainty of less than 0.01 five years after the addition of the larger detector.

Research groups in Japan have been active in the field of antineutrino physics. The most prominent Japanese experiment is the Kamioka Liquid-scintillator Anti-Neutrino Detector (KamLAND). The detector for this experiment consists of 1000 tons of liquid scintillator monitored by 1325 17-inch photomultiplier tubes and 554 20-inch photomultiplier tubes. The detector is located in central Japan and detects antineutrinos from a number of reactor installations that have a flux-weighted average distance from the detector of 180 km (Berger 2003). The experiment is aimed at determining θ_{12}, another neutrino mixing angle.

In Brazil there is another proposed experiment similar to Double CHOOZ. A 50 ton detector will be placed 300 meters from the core and a 500 ton detector will be placed 1500 meters from the core (Anjos, et al. 2006). This is another neutrino oscillation study seeking to measure the mixing angle θ_{13}.

LLNL and Sandia National Laboratory (SNL) have had an antineutrino detector deployed at the San Onofre Nuclear Generating Station (SONGS) since April of 2003.

The active medium of this original detector (SONGS1) consists of one cubic meter of gadolinium-laced liquid scintillator. A one-half meter thick water shield and a two-centimeter thick plastic scintillator active shield surrounds the central scintillator. This active shield is triggered when cosmic muons pass through the scintillators. Figure 1.4 is an illustration of this detector configuration.

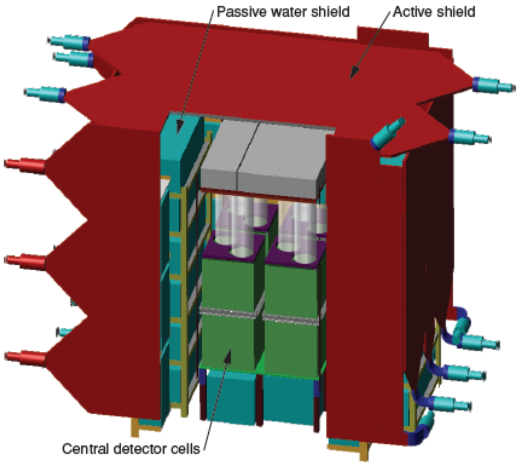

Figure 1.4: The SONGS1 detector

The data is subject to a series of "cuts" to eliminate the background signal from the valid antineutrino counts. Cuts are based on the energy of both the prompt and delayed signal, the time between the prompt and delayed signals, and the time since the last muon count. The detector is located in the tendon gallery of the containment structure for unit 2. The red circle in figure 1.5 shows the location of the SONGS1 detector relative to the reactor core.

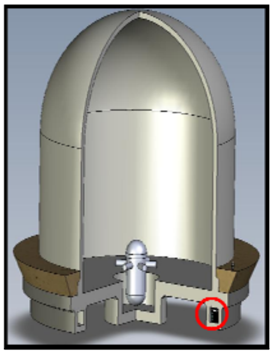

Figure 1.5: Location of the SONGS1 detector

The SONGS1 detector monitored the entirety of cycle 13 and part of cycle 14 of unit 2. The results showed that the detector was able to detect fluctuations in the power level of the reactor core based on antineutrino count rate (Bernstein, et al. 2006) (Bernstein, et al. 2007b).

In August 2007, the SONGS1 detector was upgraded to include a solid scintillator designed and built by SNL. The new detector replaced half of the liquid scintillator cells. The reason for considering a solid scintillator is that it does not have the spill or flammability risks of the liquid scintillator. The solid element consists of layers of plastic scintillator with gadolinium-painted mylar sheets placed between them. Figure 1.6 shows the SONGS1 detector with the solid scintillator element included.

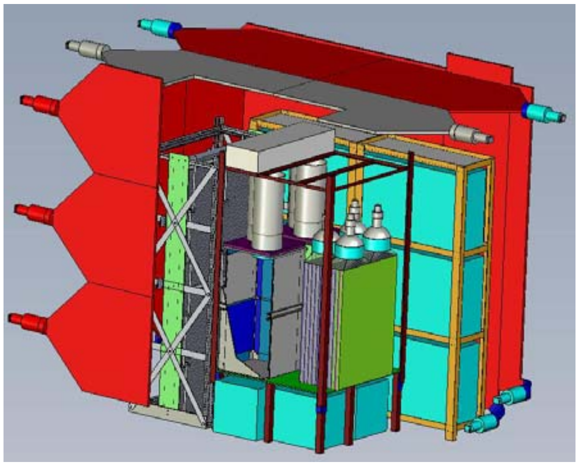

Figure 1.6: SONGS1 detector with solid scintillator element

In addition to the upgrade of the SONGS1 detector, the SONGS2 detector was deployed in August of 2007. SONGS2 is a water-based Cherenkov detector. The detector itself has two tanks: the lower tank contains gadolinium-laced water to facilitate neutron capture and the upper tank contains pure water to serve as the interface between the detector and the photomultiplier tubes. (Bernstein 2007) Figure 1.7 is a schematic of the SONGS2 detector.

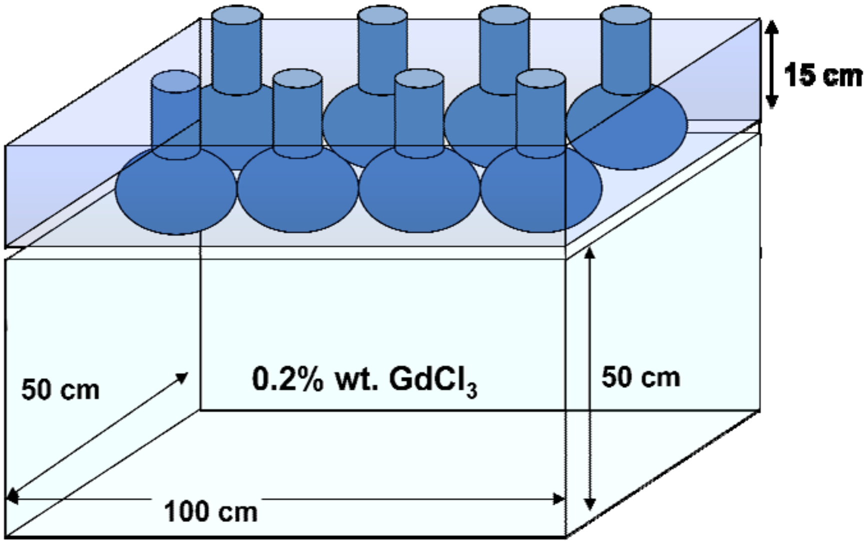

Figure 1.7: The SONGS2 detector

1.7 Past Antineutrino Simulations

There have been two previous efforts to simulate the diversion of material from a nuclear reactor. A study was performed at Los Alamos National Laboratory (LANL) utilizing the software package CINDER to deplete a reactor core and predict its antineutrino emissions. (Neito, et al. 2005) This simulation was zero dimensional with an isotopic content consistent with one third of the fuel fresh, one third of the fuel having been burned once, and one third of the fuel being twice-burned at the beginning of the cycle. The two diversion scenarios in the LANL study consisted of removing an extra 10% of the fuel in addition to the normal 33% at refueling and removing an additional 100% of fuel that would normally be replaced during refueling. The study found that removal of 10% extra fuel produced less than a 1% change in the antineutrino emissions, but a removal of an extra 100% of the fuel (66% total) resulted in a 5% higher emission rate at the start of the next cycle.

The LLNL/SNL team performed a similar zero-dimensional simulation of a reactor core using the LEOPARD code prior to the deployment of the SONGS1 detector. (Bernstein 2006) This simulation also used an isotopic content consistent with an even division of fresh, once-burned, and twice-burned fuel at the beginning of the cycle. Unlike the LANL study, there were no diversion scenarios modeled in this study. The goal of this simulation was to predict the change in antineutrino emissions that would be seen by the SONGS1 detector when it was deployed.

1.8 ORIGEN-ARP

This simulations presented in the study are performed using the Oak Ridge-developed code ORIGEN-ARP. The code is generally used in the characterization of spent reactor fuel.

ORIGEN is a time-dependent zero-dimensional fuel depletion code (Gauld, et al. 2006). It has the capability to track nuclide concentration, activity, and spectral data of the radiation emitted by the decay of nuclides during both irradiation and decay cases.

The cross-section data ORIGEN uses comes from the ENDF/B-VI, FENDL, and EAF cross-section libraries. The code has explicit fission product yields for 30 actinides. ORIGEN uses isotopic mass, power rates and times, and decay times as inputs for the depletion calculations.

Equation 1.3 is the basic equation for the change in nuclide concentration during an irradiation and decay sequence.

$$\frac{dN_i}{dt} = \sum_{\mathrm{i}} \delta_{\mathrm{ij}} \lambda_{\mathrm{j}} \mathrm{N}_{\mathrm{j}} + \sum_{\mathrm{k}} \mathrm{f}_{\mathrm{ik}} \sigma_{\mathrm{k}} \phi \mathrm{N}_{\mathrm{k}} - (\lambda_{\mathrm{i}} + \sigma_{\mathrm{i}}\, \phi) \mathrm{N}_{\mathrm{i}} \qquad (1.3)$$

where N is nuclide atom density, σ is the spectrum averaged neutron absorption cross-section, δ_{ij} is the fraction of radioactive decay from isotope j into isotope i, λ is the radioactive decay constant of the nuclide, f_{ik} is the fraction of neutron absorptions that cause isotope k to become isotope i, and □ is the space and energy averaged neutron flux. This equation can be written in the matrix form shown in equation 1.4.

$$\frac{d\vec{N}}{dt} = \underline{\mathrm{A}}\vec{\mathrm{N}} \tag{1.4}$$

The solution to this differential equation is given in equation 1.5.

$$\vec{N}(\mathrm{t}) = \mathrm{e}^{\underline{\mathrm{A}}\mathrm{t}}\vec{\mathrm{N}}_0 \tag{1.5}$$

where N_0 is a vector containing the initial concentration of each of the nuclides in the simulation.

ORIGEN solves this equation using the matrix exponential method. The method treats the exponential function as a series expansion that is shown in equation 1.6.

$$e^{\underline{A}t} = \sum_{\mathrm{m}=0}^{\infty} \frac{(\underline{\mathrm{A}}\mathrm{t})^{\mathrm{m}}}{\mathrm{m}!} \tag{1.6}$$

ORIGEN contains the matrix A with over 35,000 non-zero entries that consist of the transfer coefficients for all of the nuclides that the code can track. Nuclides can be dynamically removed from the matrix based on the comparison of their half-life to the time step. This is because the short-lived isotopes are quickly in secular equilibrium with their parent nuclei. The concentrations of the nuclides that are removed from the matrix are then solved for using the Bateman equations and the Gauss-Seidel iterative technique.

The flux used in equation 1 is derived from the power specified by the user. The relationship between neutron flux and power is shown in equation 1.7.

$$\phi = \left(1.6 \times 10^{-19} \sum_{ij} Q_{ij} N_i \sigma_{ij}\right) \frac{\mathrm{P}}{\sum_{\mathrm{i}} \mathrm{N_i} \sigma_{\mathrm{i}}^{\mathrm{f}}} \tag{1.7}$$

In the above equation, Q_{ij} is the recoverable energy from nuclide i undergoing reaction j (fission, neutron capture, etc.), σ_{ij} is the cross-section for nuclide i to undergo reaction j, P is power, and σ^f is the fission cross-section.

ORIGEN uses a predictor-corrector method to calculate the nuclide concentrations at the end of a given time step. The flux is calculated at the beginning of the time step and then used to estimate the end of time step nuclide concentrations. The end of time step flux is then calculated using the estimated concentrations and the specified power of the time step. A second depletion calculation is performed for the time step using the simple average of the beginning of time step flux and the end of time step flux. This calculation yields the nuclide concentrations that are used in the next time step. Figure 1.7 illustrates this method for the first of 4 time steps within a burn step.

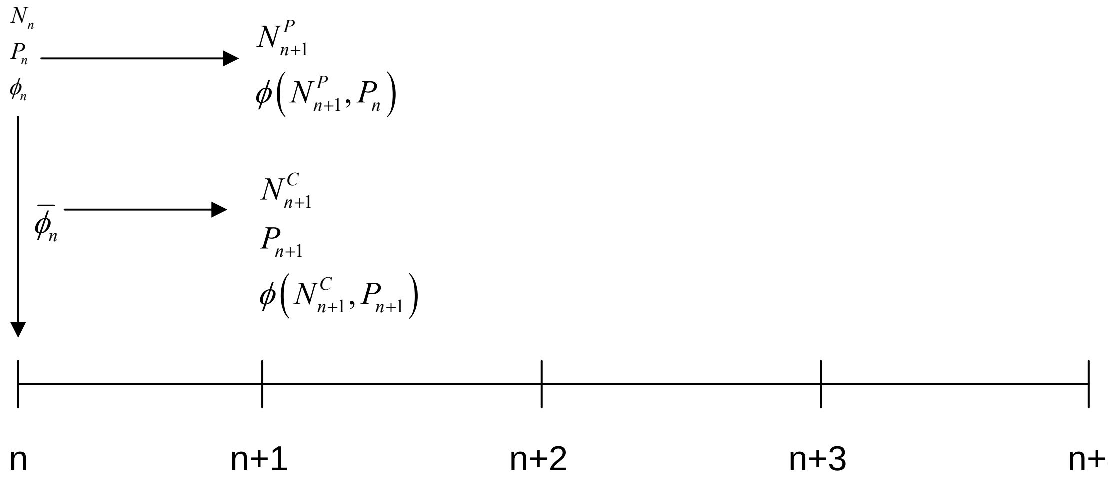

Figure 1.8: Predictor-corrector method in ORIGEN

This method gives second order accuracy. There are methods, such as 4th order Runge-Kutta, which give higher accuracy at the expense of requiring more computation time for each step in the simulation.

The Automated Rapid Processing (ARP) module generates cross-sections that are then used by ORIGEN by interpolating between precomputed libraries of certain assembly types. The interpolation is made primarily over enrichment level. By default, ARP can interpolate PWR cross-sections between enrichments of 1.5% and 5%. However, by modifying a data file, the code can extrapolate beyond those values.

2. Models

The simulations performed in this study predict the antineutrino emission rates, detector response, isotope mass density, and isotope number density based on the initial isotopics and the power levels of assemblies over a reactor cycle. The fission rates reported by ORIGEN-ARP are then processed in a spreadsheet to find the antineutrino emission rate. This can then be further processed to predict detector response. Figure 2.1 is a flow chart of the simulation methodology.

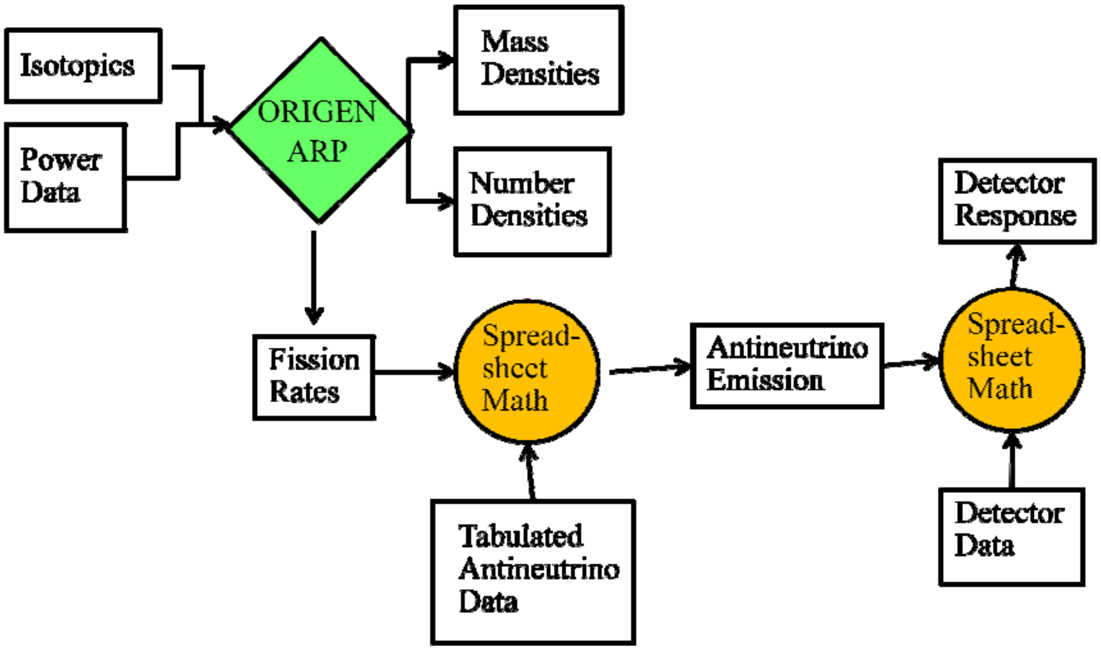

Figure 2.1: Simulation flow chart

Because the simulations are performed using ORIGEN-ARP, they are all zero-dimensional. These non-dimensional assembly simulations may be placed together to generate a pseudo two-dimensional representation of a reactor core.

All of the simulations in this study use the default 238-group neutron library in ORIGEN and the default moderator densities (0.67 for LEU, MOX, and MASLWR and 0.71 for SONGS) for the assembly libraries. The power histories used in these simulations may be found in appendix A and the physical properties of the assembly types used may be found in appendix B.

2.1 SONGS Core

To demonstrate the accuracy of the modeling technique used in this study, we have performed a direct comparison between simulated results and observed data. This is accomplished by using data provided by SONGS for the isotopic content of the fuel assemblies in unit 2 at the beginning of cycle 13. SONGS also provided the relative power densities for each assembly at 19 different times during the cycle. The data provided by SONGS is proprietary to Southern California Edison Company.

The core of SONGS unit 2 consists of 217 Combustion Engineering 16x16 assemblies arrayed in a roughly cylindrical configuration. Figure 2.2 is an illustration of a 16x16 fuel assembly.

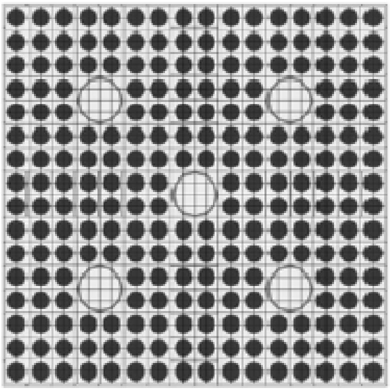

Figure 2.2: CE 16x16 PWR assembly

Approximately half of these assemblies are fresh fuel, while the rest had been burned in one or two previous cycles. Figure 2.3 shows the arrangement of the fuel in the core with blue representing fresh fuel, yellow representing once-burned fuel, and red representing twice-burned fuel.

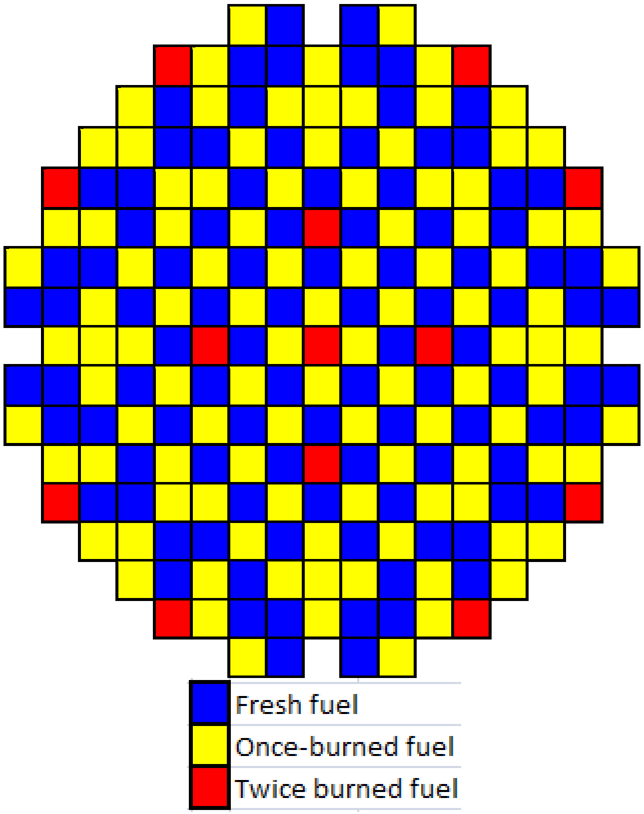

Figure 2.3: Map of the SONGS core

2.2 LEU Core

The LEU core consisted of 62 Westinghouse 17x17 assemblies with isotopics and power histories based on the final safety analysis report (FSAR) for SONGS. (SCE and SDG&E 1978) The power history data for the LEU core are displayed in table A.1. The burnup and enrichment data given for the assemblies in the FSAR could not be exactly matched, so six groups of assemblies have been developed to emulate the real data. These six groups were comprised of two types of fresh fuel, three types of once-burned fuel, and one assembly that was twice-burned. The FSAR provides relative power densities for all of the assemblies at the beginning of the cycle (BOC), middle of the cycle (MOC), and the end of cycle (EOC). Using this data, the 392-day cycle is divided into thirds with one third of the cycle length corresponding to each of those powers. This simulation represents the normal operation case for the test core and serves as a baseline for the diversion scenarios that follow. Figure 2.4 shows the spatial arrangement and enrichment data for the assemblies used in this core.

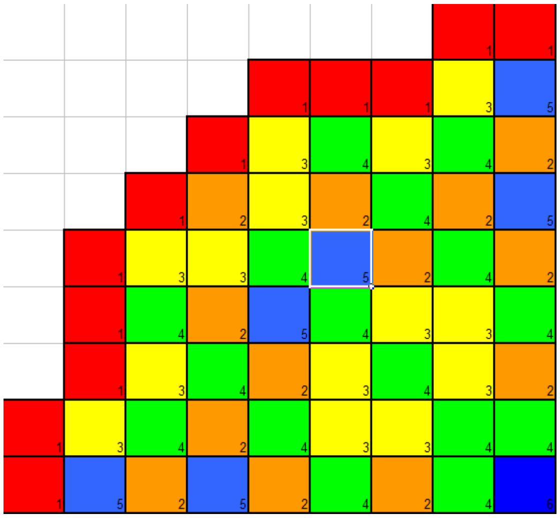

							1	1
				1	1	1	3	5
			1	3	4	3	4	2
		1	2	3	2	4	2	5
	1	3	3	4	5	2	4	2
	1	4	2	5	4	3	3	4
	1	3	4	2	3	4	3	2
1	3	4	2	4	3	3	4	4
1	5	2	5	2	4	2	4	6

🟥 1	Fresh 3.91%
🟧 2	Fresh 3.37%
🟨 3	Once Burned 4.6% (11504 MWD/MTU)
🟩 4	Once Burned 4.8% (19876 MWD/MTU)
🟦 5	Once Burned 3.91% (12368 MWD/MTU)
🟦 6	Twice Burned 3.91% (23000 MWD/MTU)

Figure 2.4: Map of the LEU core

Three scenarios are investigated to understand the effect of various diversion activities on the antineutrino spectrum of the test core. The first consists of removing five fresh 3.91% enriched assemblies and replacing them with 1.5% enriched assemblies. This adds more ^{238}U to the core, which can then be transmuted to ^{239}Pu. The enrichment value 1.5% was chosen because this is the minimum enrichment ORIGEN-ARP can model without extrapolation. This case will be referred to as scenario A. In the second case, scenario B, ten of the once-burned assemblies with the highest plutonium content are removed and replaced with 3.91% enriched fresh fuel. This represents the removal of 70 kg of ^{239}Pu from the core. The final diversion case, scenario C, utilized the same assemblies as the baseline case but the power is increased to 105% of the nominal level over the cycle. This case would have an increased neutron flux and therefore potentially more ^{239}Pu is generated.

2.2 MOX Core

The model used to simulate a MOX core was based on a benchmark of the Purdue Advanced Reactor Core Simulator (PARCS) code performed by Purdue University for the Nuclear Energy Agency. (Kozlowski and Downar 2006) This model consists of a 56-assembly quarter core, with 14 MOX and 42 LEU assemblies. The assemblies are all of the Westinghouse 17x17 design. The isotopics for this model are generated by burning the assemblies with the specified initial enrichment to the correct burnup level in ORIGEN-ARP. The power histories of the assemblies are derived from the burnup histories provided in the benchmark description. The power histories contain 20 total time steps: 5 1-day steps and 15 30-day steps for a total cycle of 455 days. Tables A.2 and A.3 display the power history for the MOX simulation in megawatts per metric ton of heavy metal. Figure 2.5 is a map of the MOX core with assembly burnup data.

Three scenarios are investigated for the diversion of material from the MOX core. In scenario A, six once-burned LEU assemblies are replaced with 1.5% enriched fresh LEU assemblies. In scenario B, five fresh MOX assemblies are replaced with 4.5% enriched LEU assemblies. The assemblies that are altered in these scenarios are labeled in figure 2.5 with a letter corresponding to the scenario. Scenario C uses the same assemblies as the baseline case but increased the power is to 105% of the nominal level over the cycle.

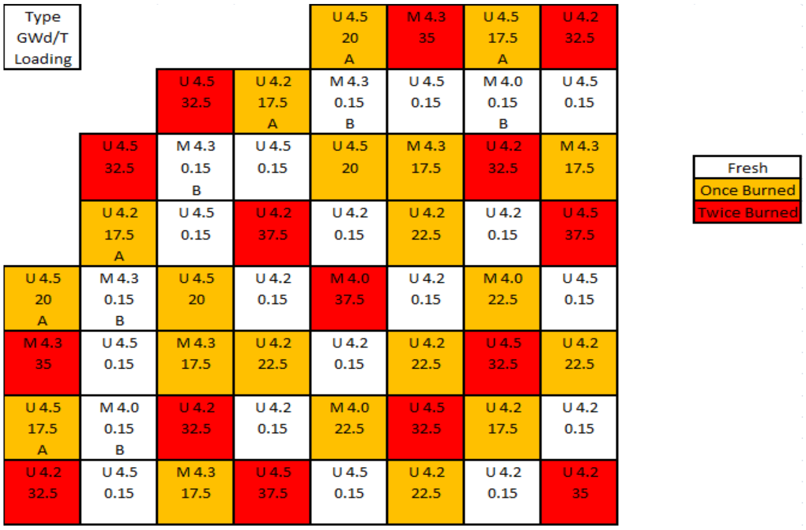

Type GWd/T Loading				🟨 U 4.5 20 A	🟥 M 4.3 35	🟨 U 4.5 17.5 A	🟥 U 4.2 32.5
		🟥 U 4.5 32.5	🟨 U 4.2 17.5 A	⬜ M 4.3 0.15 B	⬜ U 4.5 0.15	⬜ M 4.0 0.15 B	⬜ U 4.5 0.15
	🟥 U 4.5 32.5	⬜ M 4.3 0.15 B	⬜ U 4.5 0.15	🟨 U 4.5 20	🟨 M 4.3 17.5	🟥 U 4.2 32.5	🟨 M 4.3 17.5
	🟨 U 4.2 17.5 A	⬜ U 4.5 0.15	🟥 U 4.2 37.5	⬜ U 4.2 0.15	🟨 U 4.2 22.5	⬜ U 4.2 0.15	🟥 U 4.5 37.5
🟨 U 4.5 20 A	⬜ M 4.3 0.15 B	🟨 U 4.5 20	⬜ U 4.2 0.15	🟥 M 4.0 37.5	⬜ U 4.2 0.15	🟨 M 4.0 22.5	⬜ U 4.5 0.15
🟥 M 4.3 35	⬜ U 4.5 0.15	🟨 M 4.3 17.5	🟨 U 4.2 22.5	⬜ U 4.2 0.15	🟨 U 4.2 22.5	🟥 U 4.5 32.5	🟨 U 4.2 22.5
🟨 U 4.5 17.5 A	⬜ M 4.0 0.15 B	🟥 U 4.2 32.5	⬜ U 4.2 0.15	🟨 M 4.0 22.5	🟥 U 4.5 32.5	🟨 U 4.2 17.5	⬜ U 4.2 0.15
🟥 U 4.2 32.5	⬜ U 4.5 0.15	🟨 M 4.3 17.5	🟥 U 4.5 37.5	⬜ U 4.5 0.15	🟨 U 4.2 22.5	⬜ U 4.2 0.15	🟥 U 4.2 35

⬜ Fresh
🟨 Once Burned
🟥 Twice Burned

Figure 2.5: Map of the MOX core

2.4 MASLWR

The MASLWR is a reactor that is being developed at Oregon State University. The primary goal of the project is to develop a modular, economic, and passively safe small reactor for deployment domestically and abroad. (Modro, et al. 2003) The fact that the reactor is intended to be deployed oversees makes it of particular interest from a nonproliferation point of view. One feature of the design is that there is no on-site refueling, which means there is no opportunity to divert fuel during a refueling outage. As a result, the simulation performed for the MASLWR core consists only of a baseline case. This is used to define the characteristics of an antineutrino detector that could measure the power level of the core to ensure that it is at the stated level.

The proposed core of MASLWR differs from that of a traditional power reactor in size. There are 24 assemblies rather than hundreds and these assemblies are half the height of traditional PWR assemblies. This smaller core is possible because MASLWR is designed to produce 150 megawatts rather than the 3.46 gigawatts that a reactor like SONGS produces. The assemblies used in MASLWR differ from traditional PWR fuel due to the use of 8% enriched LEU rather than ~5% enriched LEU. Figure 2.6 is a diagram of the proposed MASLWR core. The lack of on-site refueling also causes a difference from traditional fuel due to the fact that all of the fuel in MASLWR is fresh at the beginning of the cycle.

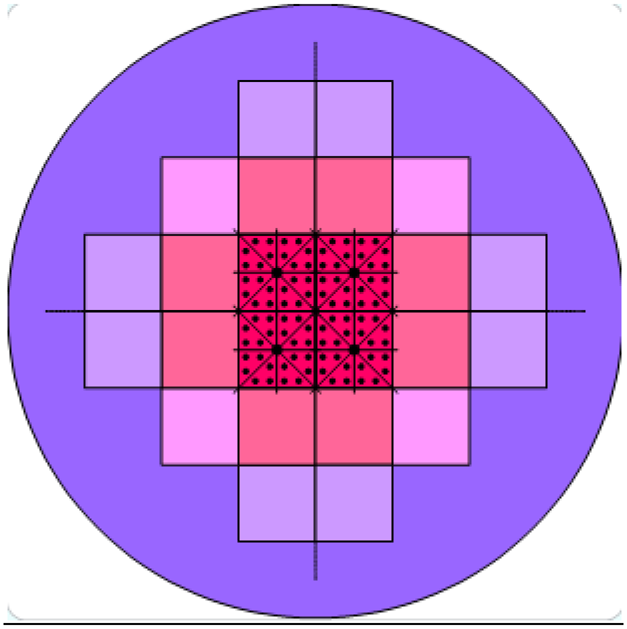

Figure 2.6: MASLWR Core

While all of the fuel is fresh at the beginning of the cycle, not all of the fuel is identical. Assemblies are loaded with varying amounts of burnable poisons depending on their position in the core in order to flatten out the power profile. (Soldatov 2008) This affects the power histories of the assemblies such that while there are six assemblies in the quarter core, there are only four unique power histories.

2.5 Error Analysis

Error is introduced in the simulation in four ways: uncertainty in the input data, the errors in the simulation package, uncertainty in the antineutrino emissions of the fission products, and the statistical uncertainty of the detector. The first of these arises due to the fact that the power of a reactor is not known precisely, rather it is known to within a given margin. This leads to an uncertainty in the neutron flux in the core, which in turn leads to an uncertainty in the isotopics of the fuel assemblies. The only way to be sure of the exact contents of a fuel rod is to perform a destructive analysis, and even that method will have an uncertainty introduced by the experimental procedure used. Because no data on the uncertainty level of the input data is available, this uncertainty will not be considered in the analysis of results.

ORIGEN-ARP creates an error due to uncertainty of branching ratios in fission. Studies have been performed to evaluate this error in specific cases by performing destructive analysis on fuel pins of reactors that have been simulated with the software. (Hermann, et al. 1995) This error has proven to be small and the code has been validated for use by regulatory bodies. This error is not considered in this analysis because this study is concerned with a detector's ability to see abnormal operations in the core. The simulation of the SONGS core and its validation against observed antineutrino data was undertaken in order to show that ORIGEN-ARP could predict the antineutrino emission rate within the uncertainty of the detector itself.

There have been a number of experiments conducted to measure the antineutrino spectra of fission products. (Huber and Schwetz 2004) (Schwetz 2004) (Avignone III and Greenwood 1980) These experiments strive to provide either a formula or table that can be used to convert from fission rate to spectral antineutrino emission rate. These studies provide relative errors associated with their data and this uncertainty is factored into this analysis.

Finally, there is uncertainty associated with the detector itself. This uncertainty is statistical in nature and is related to the total counts. This analysis reports simulated detector results with a one standard deviation uncertainty.

In order to predict the required properties of a detector to measure a given change in the antineutrino count rate, the relative error must be no greater than 50% of the relative difference between the normal and abnormal count rates. The detector properties can be expressed in a single parameter as shown in equation 2.1.

$$\zeta = \frac{\varepsilon N V}{4\pi r^2} \tag{2.1}$$

where ε is the intrinsic detector efficiency, N is the proton density, V is the detector volume, and r is the distance between the detector and the reactor core. ζ has the units of cm^{-2}. Detector count rate can be expressed as a function of this quantity as shown in equation 2.2.

$$\dot{C}(\zeta) = \zeta \sum_i \int \sigma(E)\, \dot{F}_i \bar{\nu}_i(E) dE \tag{2.2}$$

where σ is the cross-section of the inverse-β decay reaction of a proton, $\dot{F}_i$ is the fission rate of isotope i, and ν_i is the antineutrino spectrum of the products of the fission of isotope i. The relative error of a detector can be predicted by combining the counting uncertainty with the uncertainty in the antineutrino spectrum as shown in equation 2.3.

$$RE(\zeta) = \frac{\sqrt{\sum_i \left[(\dot{F}_i \int \sigma(E) \delta_i(E) dE)^2 \right] + \dot{C}(\zeta)}}{\dot{C}(\zeta)} \tag{2.3}$$

where δ_i is the relative error of the antineutrino spectrum of the products of the fission of isotope i. The values of $\delta_i(E)$ come from the experimental measurements of β spectra of fission products of fuel isotopes which are converted to antineutrino spectra. Because it is difficult to measure low energy β particles, the relative errors of those measurements are higher than those of high energy β particles. This causes a corresponding increase in relative error of the antineutrino spectra as the energy of the particles increase.

3. Numerical Results

This chapter will cover the results of the ORIGEN-ARP simulations. All of the spectral plots use data based on the SONGS1 detector (1 m^3 of mineral oil-based liquid scintillator at a standoff distance of 25 m). The results will be divided into sections covering the validation of the simulation method against SONGS data, the LEU core, the MOX core, the comparison of LEU versus MOX, and the MASLWR core.

The simulated antineutrino emission rate plots are shown without error bars in this chapter. The errors due to uncertainty in the emission of the fission products and the counting statistics will be addressed in the next chapter when the requirements for detectors to sense the changes in the antineutrino signature will be discussed. The spectral plots based on the simulated response of the SONGS1 detector are shown with the error bars based on the properties of that device.

3.1 SONGS Validation

The results of the SONGS simulation is shown in figure 3.1 plotted with observed data from the SONGS1 detector. The data are displayed as a continuous cycle, however the detector data covers the end of cycle 13 and the beginning of cycle 14 of SONGS unit 2.

In figure 3.1, the simulation is the blue line and the observed data are the points with uncertainty bars. This plot shows that the simulated data follows the trend of the observed count rates and generally falls within the uncertainty of the detector. This shows that the simulation method used in this study provides results that match observed data within the limitations of current detector technology.

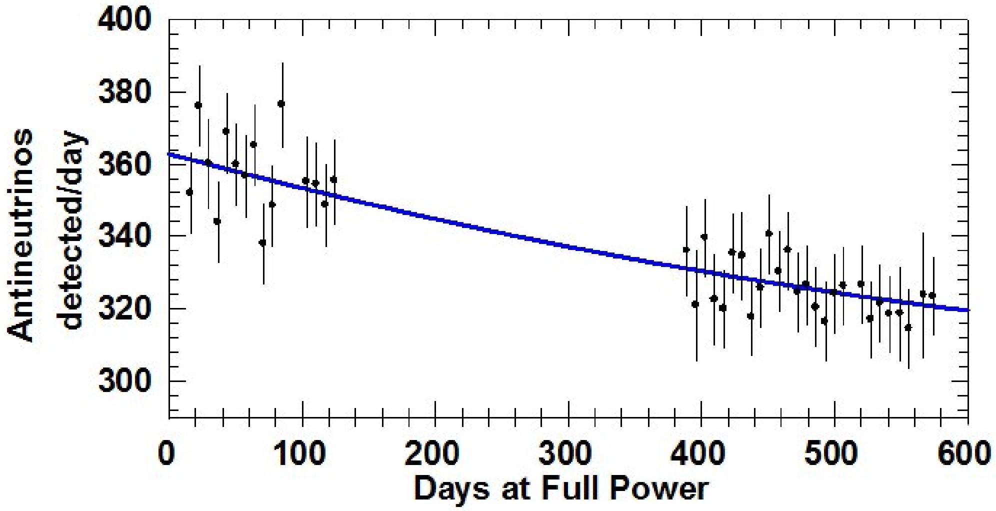

Figure 3.1: Comparison of simulated and observed SONGS data

3.2 LEU Results

Figure 3.2 shows percentage of fissions due to each of the four main fuel isotopes in the LEU core for the baseline case.

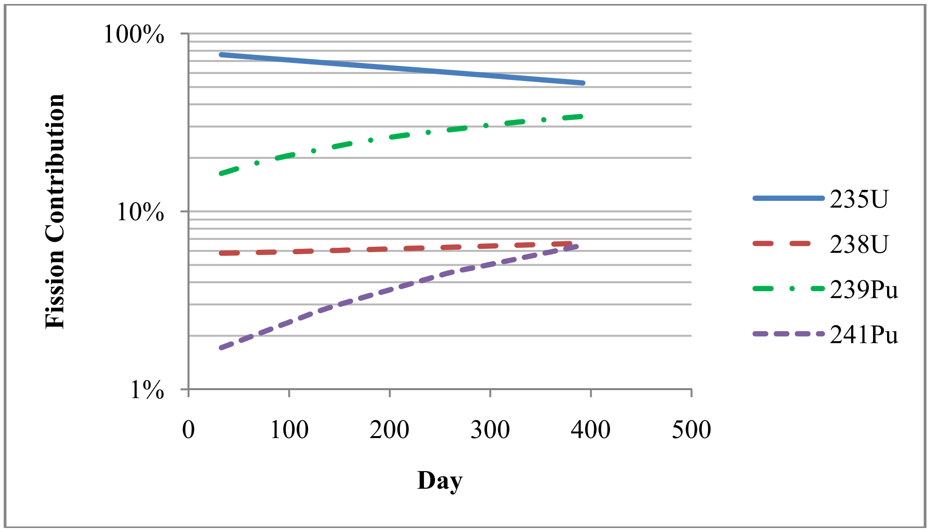

Figure 3.2: Isotopic fission contributions for a LEU core

The above plot (figure 3.2) shows the characteristic depletion curves for LEU PWR fuel. The contribution to fission from ^{235}U decreases linearly as it is burned out of the fuel, while both ^{239}Pu and ^{241}Pu increase significantly as they are created through neutron absorption reactions. The fission contribution of ^{238}U increases slightly, but is largely unaffected due to its low thermal fission cross-section.

Figure 3.3 shows the antineutrino emission rate for all of the simulated cases of the LEU core.

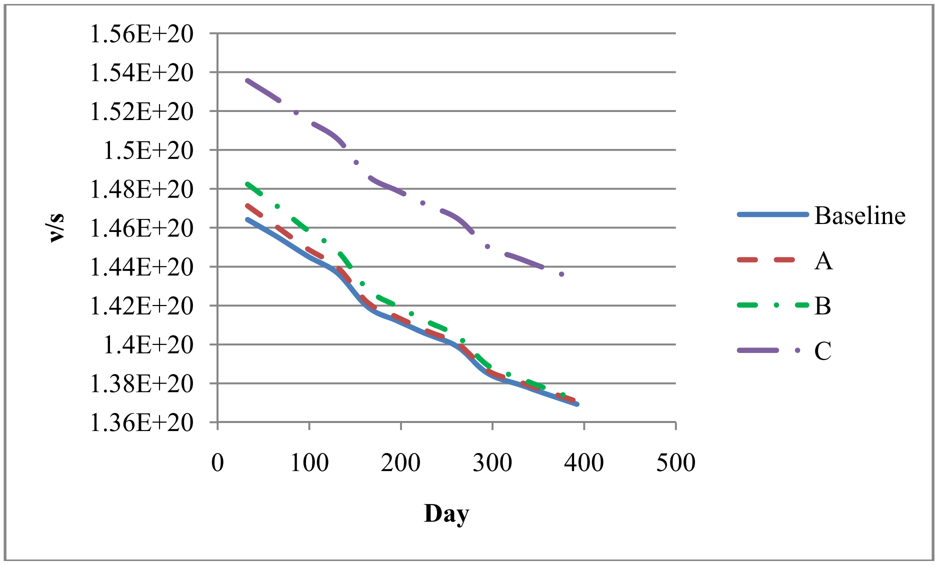

Figure 3.3: Antineutrino emission rate of an LEU core

The sudden changes in slope in the above plot correspond to the discontinuities in the power levels used in the simulation. Scenarios A and B show the trend of converging with the baseline case towards the end of the cycle. Scenario C, which consists of the power being 105% of the baseline, shows a 5% increase in antineutrino emission rate over the baseline.

Figure 3.4 shows the differences of the antineutrino spectra of the diversion scenarios relative to the baseline as would be measured with a detector with the properties of SONGS1. The fission rate data used to generate these spectra is from 32 days into the cycle.

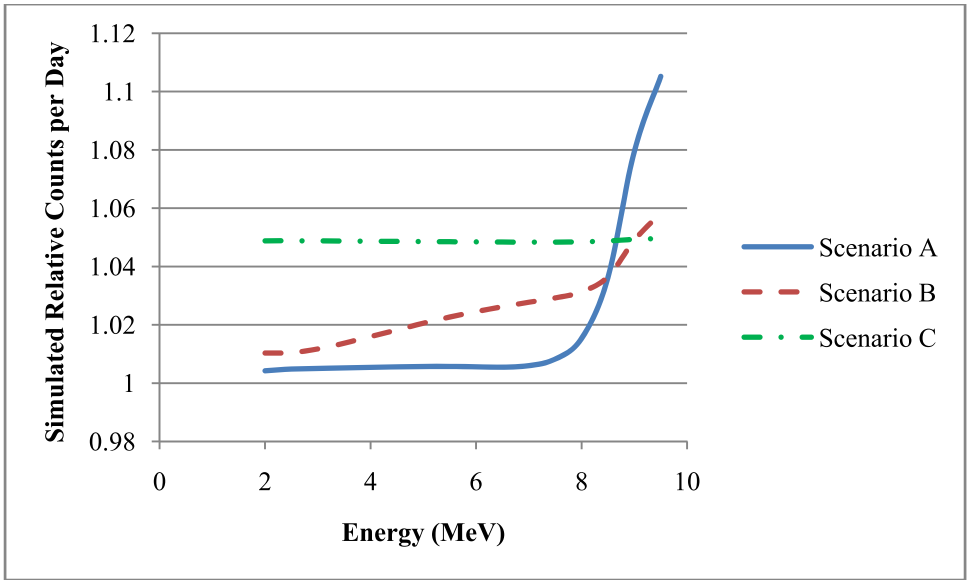

Figure 3.4: Antineutrino detector response for a LEU core relative to baseline

This plot shows that there are only small differences created in the antineutrino spectrum by the diversion scenarios. There is more than a 10% increase of 9.5 MeV antineutrinos by scenario A compared to the baseline, however this is the region of the spectrum where the least number of total antineutrinos are emitted, making this difficult to measure.

3.3 MOX Results

The isotopic fission contributions for the MOX core are shown in figure 3.5. There are important differences between the MOX and LEU depletion curves. Compared with a LEU core, both of the plutonium isotopes start as higher fractions of the total fission rate and then increase to higher levels at EOC. By EOC, ^{239}Pu constitutes the largest percentage of the total fissions and ^{241}Pu represents over 10% of the total fissions.

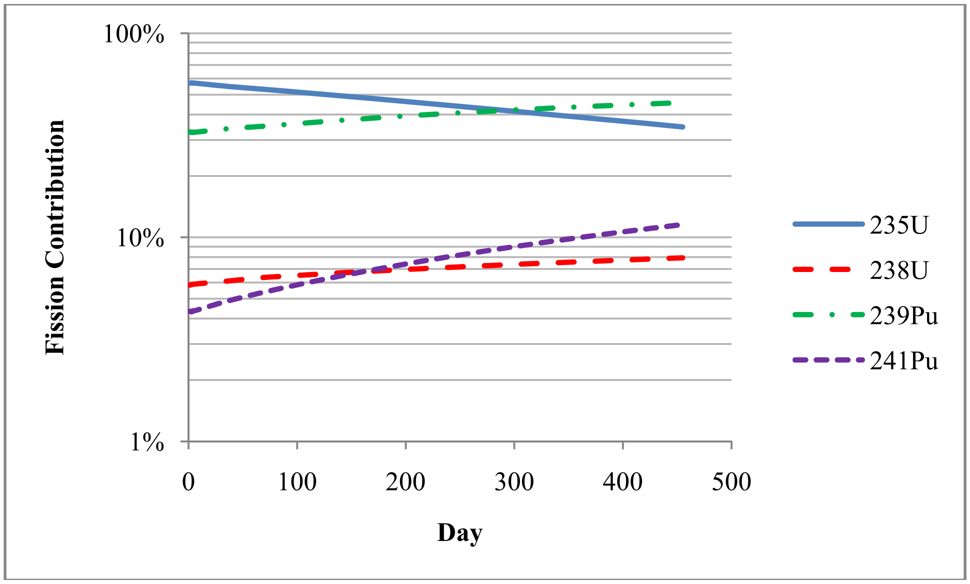

Figure 3.5: Isotopic fission contributions for a MOX core

Figure 3.6 shows the antineutrino emission rates of the baseline and diversion scenarios of the MOX core.

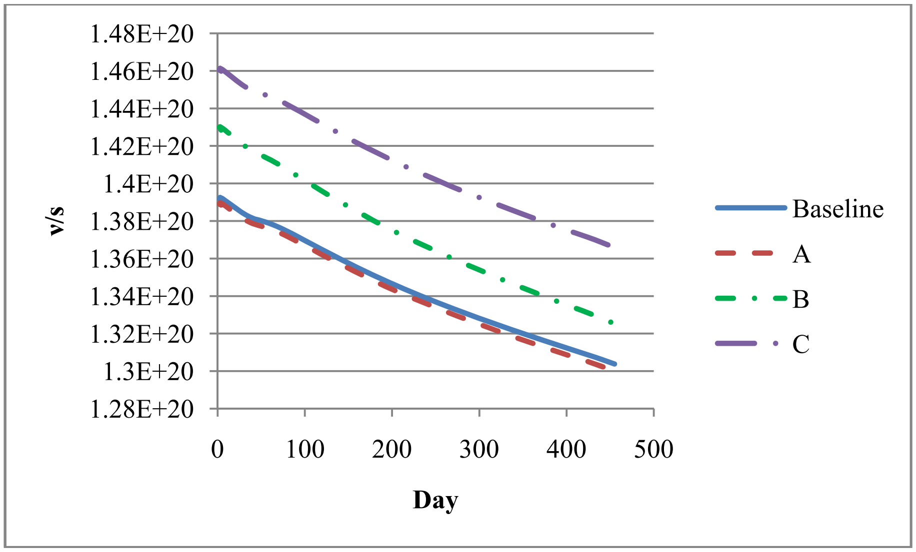

Figure 3.6: Antineutrino emission rates of a MOX core

The MOX plot is noticeably smoother than the corresponding LEU plot due to smoother time dependence of the power. Scenario B also shows a much larger difference from the baseline than in the LEU case, which is due to the much larger amount of plutonium removed in the MOX simulation. However, like in the LEU simulation, the antineutrino emission rate of scenario B does tend toward the baseline case at the end of the cycle.

Figure 3.7 shows the relative difference of the antineutrino spectra of diversion scenarios to the baseline case as seen by a detector similar to the SONGS1 detector.

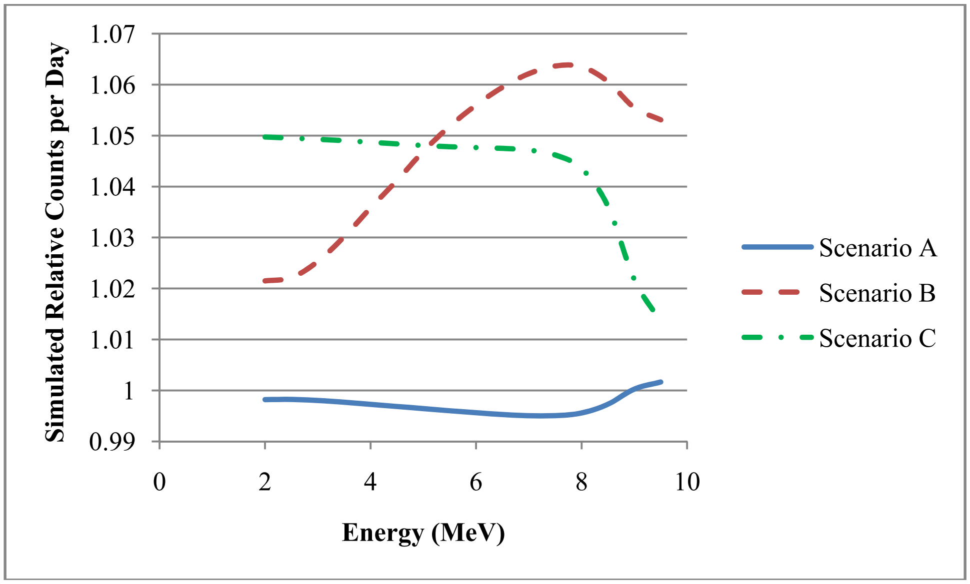

Figure 3.7: Antineutrino detector response for a MOX core relative to baseline

The differences in the spectra caused by the diversion scenarios is slight, but the difference between scenario B and the baseline is larger than it is for the LEU core. It is of note that scenario C for the MOX core approaches the baseline case at high energies. This is different than what was seen in the LEU simulation, where the emissions for scenario C were uniformly higher than the baseline.

3.4 LEU and MOX Comparison

Because the cores in the LEU and MOX simulations operated at different power levels, the data used to compare them are normalized by dividing by the power. The SONGS simulation was used to represent a LEU core for these comparisons due to its being based on a currently operating reactor rather than a 30-year-old prediction of a reactor. Figure 3.8 shows the antineutrino emission rate per megawatt for both an LEU and a MOX core.

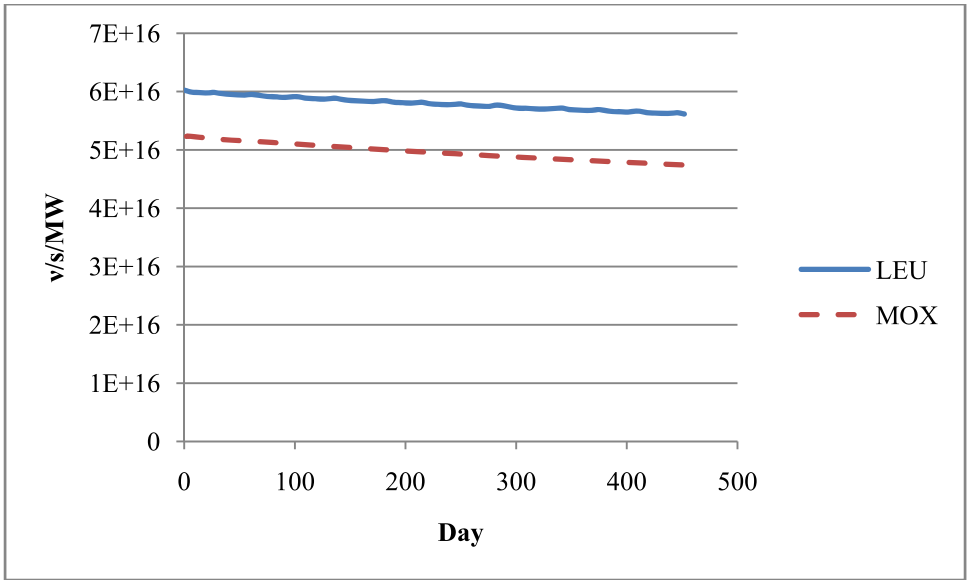

Figure 3.8: Comparison of antineutrino emissions of a LEU and MOX core

The MOX core emits fewer antineutrinos per megawatt than the LEU core. This is due to the increased percentage of fissile material that is ^{239}Pu, which emits less antineutrinos per fission.

Figure 3.9 compares the spectra of LEU and MOX cores at the end of a cycle.

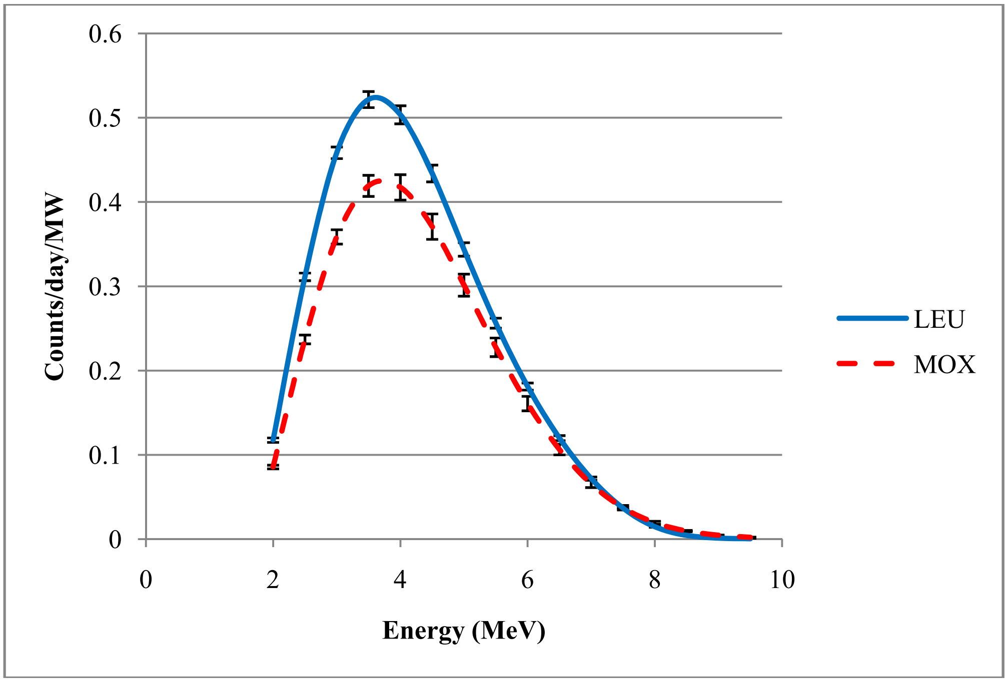

Figure 3.9: Comparison of the spectra of a LEU and MOX core at EOC

An interesting feature of the above plot is that at approximately 8 MeV, the two curves intersect each other. This behavior could potentially be used to differentiate between two reactors with different fuel types, assuming a detector with sufficient sensitivity.

3.5 MASLWR Results

The lower power of the MASLWR core relative to a typical PWR causes a lower antineutrino emission rate. Figure 3.10 shows the emission rate as a function of time for the MASLWR core.

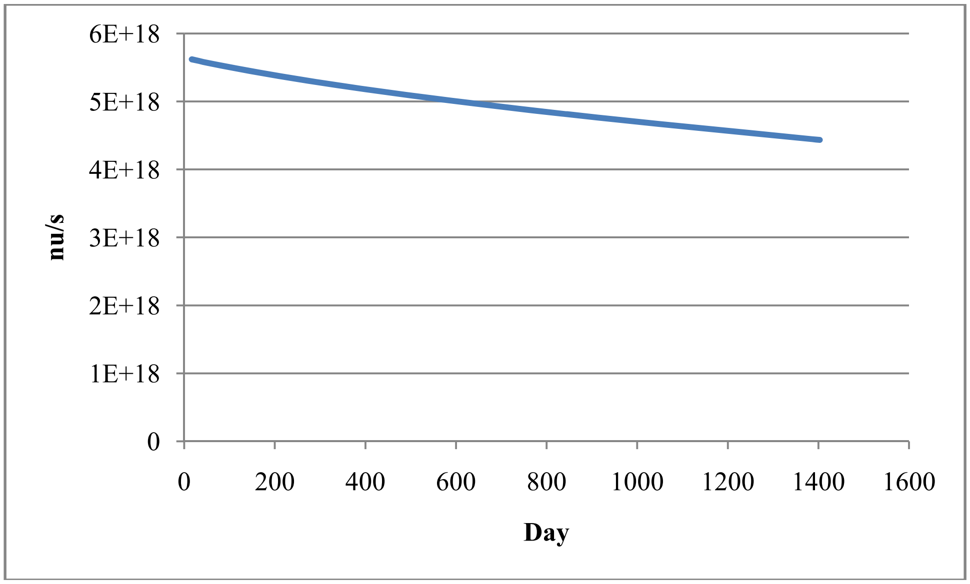

Figure 3.10: Antineutrino emission rate of the MASLWR core

The decrease of 22% in the antineutrino emission rate over the cycle is greater than what is seen in the typical PWR. The difference is due to the greater length of the cycle employed by MASLWR when compared to PWRs that utilize a traditional refueling schedule. When compared to the antineutrino emissions of SONGS over the length of the SONGS cycle, the MASLWR emission rate decreases 2% more than SONGS. The lower power density and lower relative abundance of ^{238}U when compared to SONGS also creates a lower neutrino emission rate per megawatt. Figure 3.11 illustrates the difference. Figure 3.12 displays the fission contributions of the fuel isotopes in the MASLWR core. The contribution from ^{238}U ranges between 1.3% and 2.4%, as compared to 4.7% and 7.7% in SONGS.

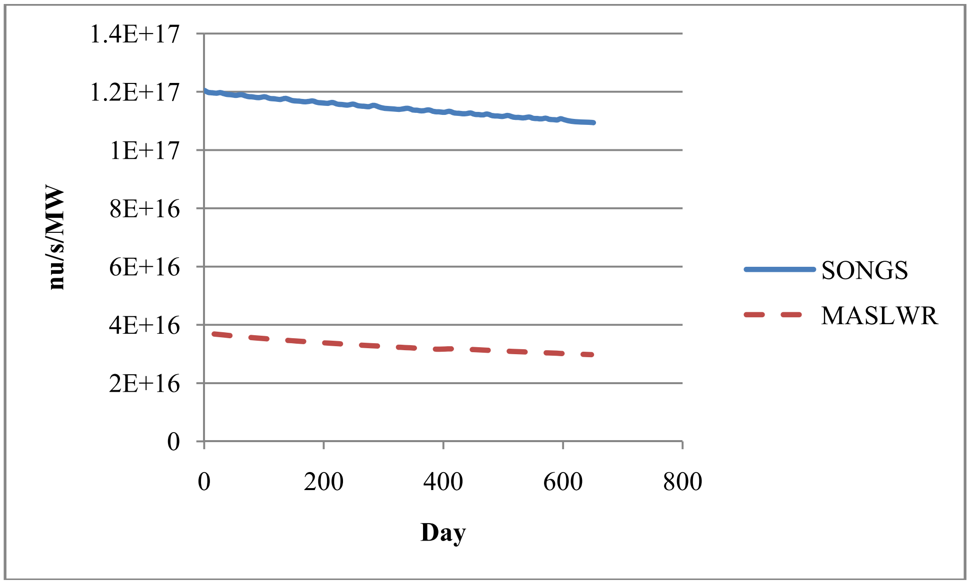

Figure 3.11: Neutrino emission rates per MW for SONGS and MASLWR

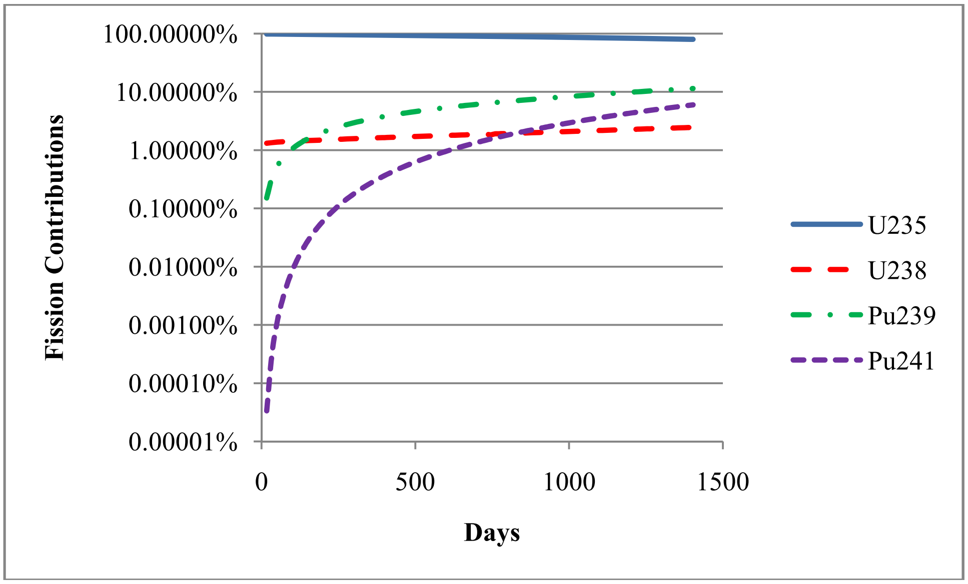

Figure 3.12: Isotopic fission contributions for MASLWR

4. Discussion

This section will address the properties that would be required for a detector to sense the differences in antineutrino signatures shown in the previous chapter. The quantity of interest for the sensitivity of a detector is the relative error it would have in a given scenario. In addition to the ζ factor described in chapter 2, relative error is also impacted by the count time of the detector. In this chapter, the plots will include curves for integration times of 1 hour, 1 day, and 30 days. The fission rates used to generate plots of relative error in the detector response are the EOC values of the simulations. EOC is used because the antineutrino emission rate is at its minimum for the cycle at that point, causing the counting error to be at its most significant.

When relative error is plotted as a function of an individual detector property, the other factors that contribute to ζ are the values of the SONGS1 detector unless otherwise stated.

4.1 Diversion Scenario Analysis

Figure 4.1 shows the relative error of the antineutrino detection rate for the LEU core based on the SONGS FSAR as a function of ζ.

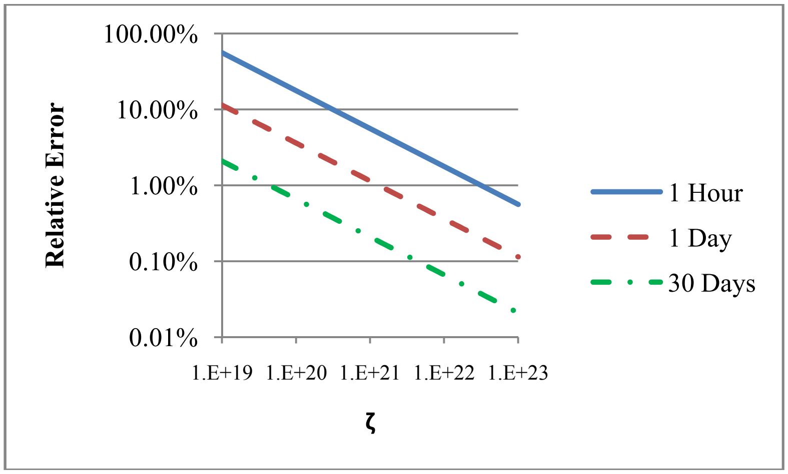

Figure 4.1: Relative error of a LEU core as a function of ζ

At EOC, scenarios A, B, and C had antineutrino emission rate differences of 0.1%, 0.16%, and 5% compared to the baseline case. To detect the addition of fertile targets (scenario A), a ζ value of 1.75E22, 5.24E23, or 1.26E25 would be required for a count time of 30 days, 1 day, or 1 hour. For a 100% efficient mineral oil detector with a standoff distance of 25 m, these ζ values correspond to volumes of 2.04E7 cm^3, 6.11E8 cm^3, and 1.47E10 cm^3. To obtain the ζ values necessary to detect the removal of plutonium-rich assemblies, the detector volumes would have to be 7.97E6 cm^3, 2.39E8 cm^3, and 5.74E9 cm^3. The required volumes of a detector to discern the reactor running at 105% power are 8153 cm^3, 2.45E5 cm^3, and 5.87E6 cm^3. Figure 4.2 shows relative error as a function of detector volume for such a detector. These results are displayed in tables 4.1, 4.2, and 4.3.

Table 4.1: Detector properties required to measure the addition of fertile targets

Integration Time	ζ (cm^{-2})	Volume (cm^3)
30 days	1.75E22	2.04E7
1 day	5.24E23	6.11E8
1 hour	1.26E25	1.47E10

Table 4.2: Detector properties required to measure the removal of plutonium-rich assemblies

Integration Time	Volume (cm^3)
30 days	7.97E6
1 day	2.39E8
1 hour	5.74E9

Table 4.3: Detector properties required to measure a 5% increase in power

Integration Time	Volume (cm^3)
30 days	8153
1 day	2.45E5
1 hour	5.87E6

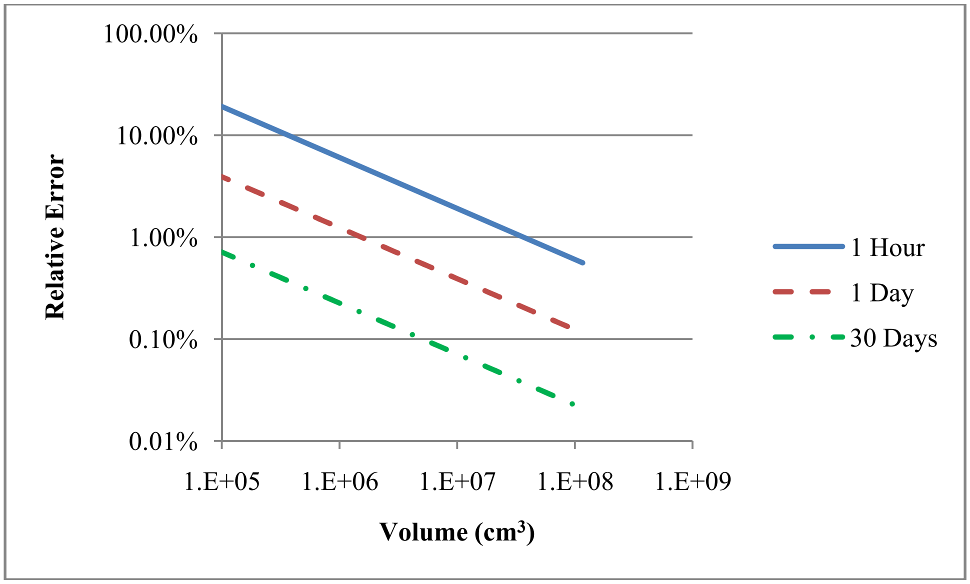

Figure 4.2: Relative error for a LEU core as a function of volume

This data shows that even with a 100% efficiency, a detector would have to be an order of magnitude larger than the SONGS1 detector to differentiate scenarios A and B from the baseline case. The difference is significantly larger when one takes the actual efficiency of the SONGS1 detector into account. However, scenario C is detectable using the SONGS1 detector characteristics.

The ζ data may also be used to plot other properties a detector would require to measure the difference in the antineutrino emissions of the diversion scenarios. Figure 4.3 shows the relative error as a function of the efficiency of a 1 m^3 mineral oil detector with a standoff distance of 25 m. This plot shows that a detector with properties similar to the SONGS1 would never be able to discern scenario A from the baseline case because even with an integration time of 30 days, the relative error does not reach the required .05% at 100% efficiency. The relative error also stays higher than would be required to detect scenario B. However, scenario C would be detectable by either 1-day or 30-day integration times.

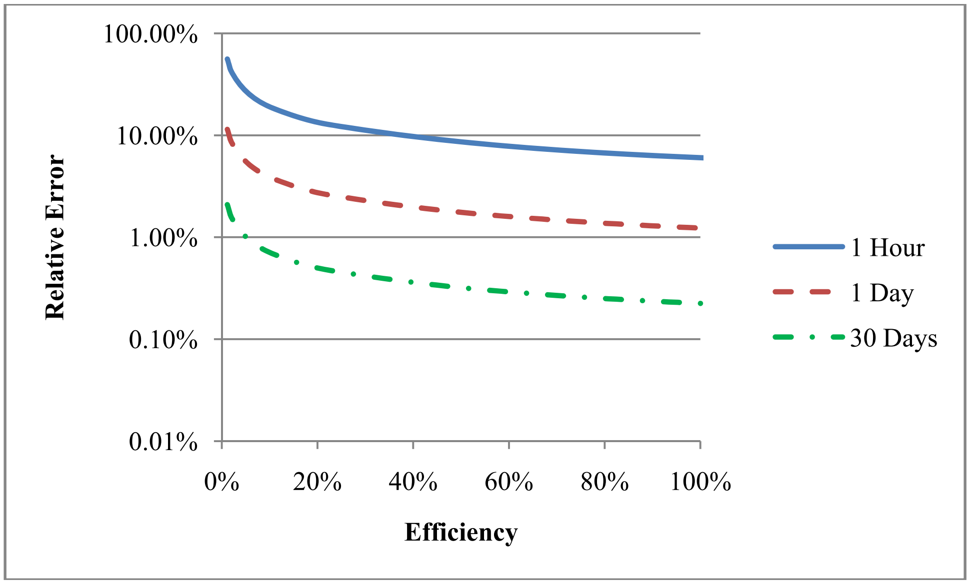

Figure 4.3: Relative error as a function of efficiency for a LEU core

When compared to the LEU data, the MOX core data yield a relative error 3.2% higher for any value of ζ. Given that the isotopics of the two reactors are very different and that the MOX core operated at 28% lower power than the FSAR core, this shows that the relationship between relative error and ζ is largely insensitive to small differences between similar reactors. The ratio of the relative errors is invariant over the range of ζ. This shows that the ratio of relative errors of antineutrino detection rates is insensitive to the value of ζ, even for reactors of different fuel types.

In addition to the magnitude of the antineutrino emission, the slope of the detection rate over the cycle can be used to verify the normal operations of a reactor. The decrease in antineutrino emissions is caused by the increased amount of plutonium relative to the amount of uranium. Because of this causation, the slope is effectively a measure of fuel depletion. If the slope of the antineutrino rate of a cycle is different than it was for the previous cycle, it is an indication that the fuel loading the beginning of the current cycle is not the expected loading for normal operations.

4.2 Power Monitoring Analysis

Both the SONGS and MASLWR simulations provide insights into the applicability of antineutrino detectors to power monitoring of nuclear reactors. They also provide a contrast in both scale and possible design of detectors used in a regime. The SONGS simulation represents a large core with preexisting facilities, and therefore possible detector locations, built around it. However, the MASLWR is a small core that is still in the design phase. This means that there is a possibility to place the detector much closer to the core and even to add it to the overall facility design.

Figure 4.4 shows the relative error as a function of ζ for the SONGS core.

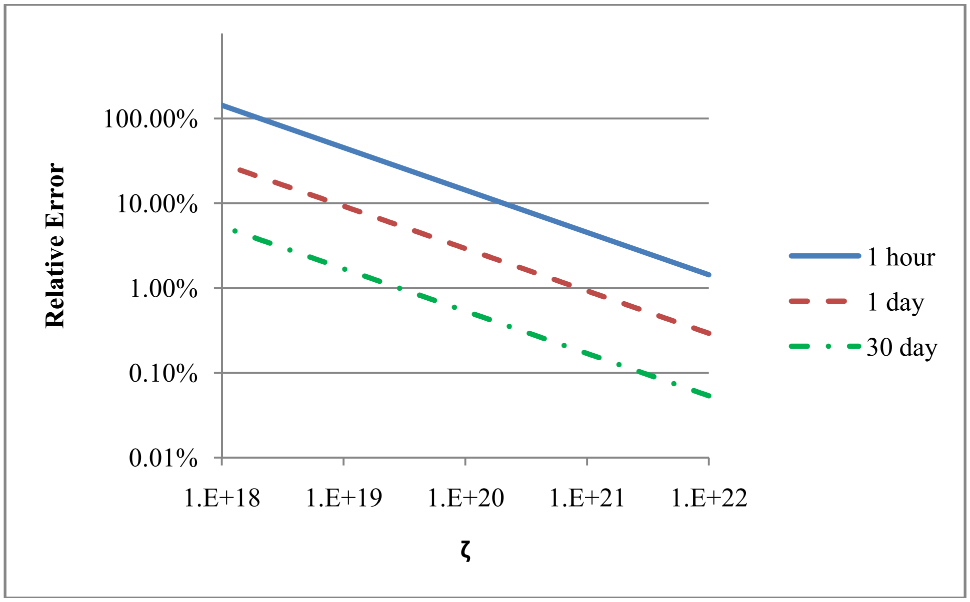

Figure 4.4: Relative error as a function of ζ for the SONGS core

This figure shows that it is possible to obtain the daily average power level of the SONGS core to a 1% uncertainty with a ζ value of 10^{21}. This corresponds to a standoff distance of 7.68 m for the SONGS1 detector. If the detector remains at its current location, its volume must be 10^7 cm^3, an increase of a factor of 10.

Figure 4.5 shows the relative error as a function of ζ for the MASLWR core.

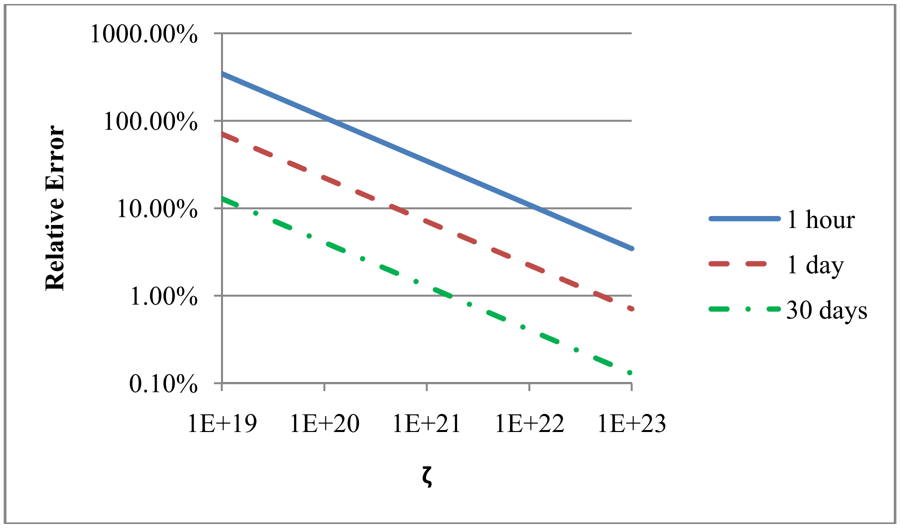

Figure 4.5: Relative error as a function of ζ for the MASLWR core

Table 4.3 shows the corresponding efficiency, volume, and standoff distance for a detector with all other properties identical to the SONGS1 detector.

Table 4.4: Properties required of a SONGS1-type detector monitoring MASLWR

RE (1 Hour)	ζ	Efficiency	Volume (cm^3)	Standoff (cm)
346.24%	1E+19	0.007%	679.0	7675.4
244.83%	2E+19	0.015%	1358.0	5427.3
154.84%	5E+19	0.037%	3394.9	3432.5
109.49%	1E+20	0.075%	6789.9	2427.2
77.42%	2E+20	0.149%	13579.8	1716.3
48.97%	5E+20	0.373%	33949.4	1085.5
34.62%	1E+21	0.747%	67898.8	767.5
24.48%	2E+21	1.494%	135797.6	542.7
15.48%	5E+21	3.734%	339494.0	343.3
10.95%	1E+22	7.469%	678988.0	242.7
7.74%	2E+22	14.938%	1357976.0	171.6
4.90%	5E+22	37.344%	3394940.1	108.5
3.46%	1E+23	74.689%	6789880.1	76.8

Based on the above data, a detector identical to SONGS1 could determine the hourly average power of MASLWR to a relative error of less than 5% with a standoff distance of approximately 1 m. The high relative error at such a close distance is due to the lower fission rate within the MASLWR core. Possible ways of improving the performance of an antineutrino detector for MASLWR will be discussed in the next chapter.

5. Conclusion/Future Work

Antineutrino detectors have the potential to play a role in reactor safeguards regimes. One of the keys to improving their effectiveness is to decrease the relative error of the measurements that they provide. There are several ways to decrease this relative error.

A possible method of decreasing this relative error would be to obtain more accurate measurements of the β spectra of the fission products of fuel isotopes. This would decrease the uncertainty associated with the antineutrinos emitted after each fission.

There are several steps that can be taken in the design of the detector itself to reduce its relative error. These steps would increase the value of ζ for the detector. As shown in equation 2.1, there are 4 quantities that contribute to ζ: the detector efficiency, the proton density of the detection medium, the volume of the detector, and the standoff distance from the reactor.

The proton density of the detection medium can be changed by using different materials in the detector. Hydrogenous solids, such as polyethylene, provide a higher concentration of protons than liquid scintillators.

The denominator of ζ can be altered by changing the solid angle subtended by the detector. This is particularly of interest in the case of MASLWR, where these new detector designs could be factored into the design of the plant itself. Figure 5.1 shows a schematic of the proposed MASLWR design.

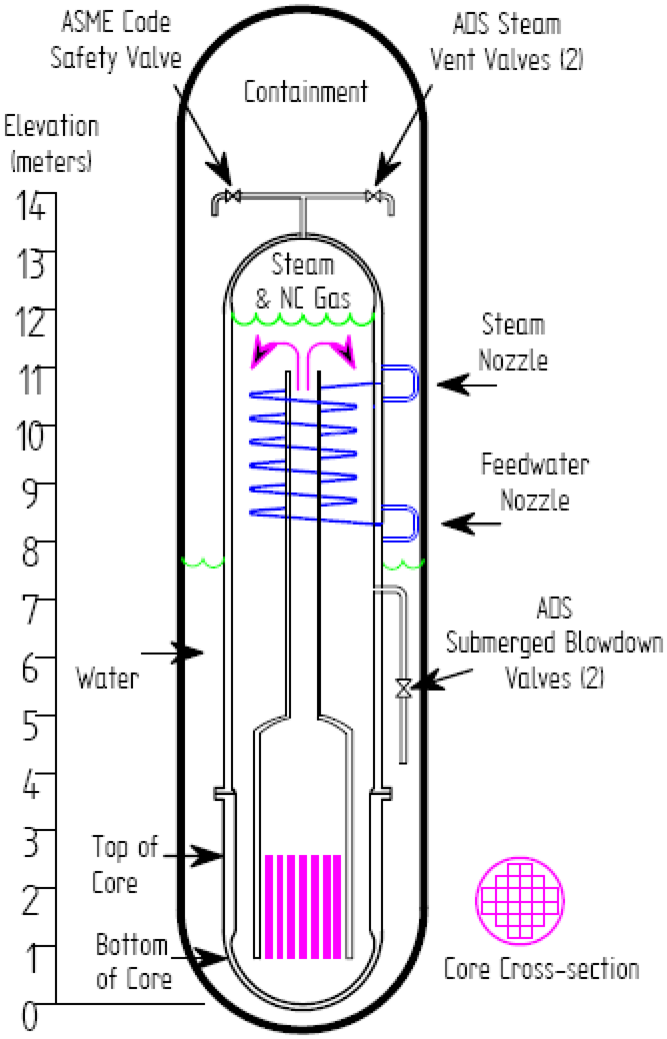

Figure 5.1: Proposed MASLWR design

One possibility to improve the performance of an antineutrino detector in this plant design would be to section off a portion of the water in the outer containment and convert it to an annular Cherenkov detector. This would involve adding gadolinium to that section of water and placing photomultiplier tubes around the annulus. This design would increase the value of ζ by ensuring that more of the antineutrinos would pass through the detection medium.

In the course of this study, ORIGEN-ARP has proven to be an accurate tool for predicting the fission rates required to derive the antineutrino emission rates of reactors.

The code provides data that can be easily converted into antineutrino emission rates through the use of tabulated data. As was shown in the SONGS benchmark, the resulting prediction of detector count rate falls within the uncertainty of observed data.

Two detection methods for measuring abnormal operating conditions were examined in this study: comparing total count rate and comparing spectra. The spectral differences between the baseline and the diversion are so slight that current detection technology cannot resolve it. However, the total count rate comparison was more promising. The scenario in which the reactor operated at 105% of nominal power generates a large enough difference in antineutrino emission rate to be detected for both the LEU and MOX cores. The scenario that involves the replacement of fresh fuel with fertile targets produces differences of less than 1% for both core types. The removal of plutonium-rich assemblies produces a more pronounced result. In the MOX case, the diversion scenario results in a nearly 3% increase in the antineutrino emission rate over the baseline at the beginning of the cycle. This could possibly be measured with a detector with properties similar to those deployed currently. The effect of the same scenario on the LEU core is less due to the lower amount of plutonium that is removed.

There are differences in the antineutrino emissions of cores fueled with LEU and MOX. The MOX core emits 15% fewer antineutrinos per megawatt of thermal energy than the LEU core. This difference may be used to verify the fuel type of an operational reactor that is being monitored with an antineutrino detector. The MASLWR core also emits fewer antineutrinos per megawatt than a traditional LEU-fueled reactor. While this difference is of less interest from a safeguards point of view, it is a factor that must be considered when determining the properties of an antineutrino detector to monitor a MASLWR core.

This study represents the most detailed simulation of the effect of diversion scenarios on the antineutrino emissions of a reactor to date. Whereas previous studies have modeled the removal of different fractions of a core during a refueling, this study was able to predict the effects of the replacement of specific assemblies in a core. However, due to the limitations of the software used, these results only represent a patchwork of zero-dimensional simulations. Future studies could examine a true, three-dimensional model of an operational reactor to investigate such effects as different levels of control rod insertion. When performing a three-dimensional analysis, it is important to make the correct assumptions about the source distribution. The difference between an assumed uniform distribution of antineutrino sources and the distribution based on the neutron flux distribution in a cylindrical reactor can be illustrated by comparing the antineutrino flux integrals of those assumptions. Equation 5.1 is the flux integral for a uniform source and 5.2 is the integral for the cylindrical distributions.

$$\phi = N\int_0^R \int_0^{2\pi} \int_{-H/2}^{H/2} \frac{r dr d\theta dz}{4\pi(D^2 + r^2 + 2Dr\cos\theta + z^2)} \quad (5.1)$$

$$\phi = N\int_0^R \int_0^{2\pi} \int_{-H/2}^{H/2} \frac{J_0\left(\frac{\nu_0 r}{R}\right) \cos\left(\frac{\pi z}{H}\right) r dr d\theta dz}{4\pi(D^2 + r^2 + 2Dr\cos\theta + z^2)} \quad (5.2)$$

In the above equations, N is the neutrino density in the reactor core, ν_0 is the smallest zero of the Bessel function J_0, R is the reactor radius, D is the detector standoff distance from the center of the core, and r, θ, and z are the cylindrical geometry coordinates. When the equations are evaluated numerically, the flux predicted by equation 5.1 is 3.6

times greater than that predicted by the more realistic distributions used in equation 5.2. This is more extreme difference than difference that would be seen between the uniform assumption and the real answer. The most correct distribution of the antineutrino source is based on the fission distribution, which is almost constant in the radial direction.

The current state of antineutrino detector technology can provide independent verification of a reactor's on/off status and estimate the burnup of its fuel. With continued research and development, these detectors have the potential to provide data on daily or hourly average reactor power. Antineutrinos provide an observable quantity that is directly related to both the power level and isotopic content of a reactor. The particles are also impossible to mask with any shielding. These two properties make antineutrino detection a desirable component for monitoring regimes aimed at the prevention of the diversion of nuclear material from legitimate civilian power reactors to illicit weapons programs.

References

Anjos, J., et al. "Angra Neutrino Project: Status and Plans." *Nuclear Physics B (Proc. Suppl.)* 155 (2006): 231-232.

Apollonio, M., et al. "Search for Neutrino Oscillations on a Long Base-Line at the CHOOZ Nuclear Power Station." *The European Physical Journal C - Particles and Fields* 27 (2003).

Ardellier, F., et al. "Letter of Intent for Double-CHOOZ: A Search for the Mixing Angle θ_{13}." *arXiv:hep-ex/0405032* 1 (2004).

Avignone III, F., and Z. Greenwood. "Calculated Spectra of Antineutrinos from the Fission Products of ^{235}U, ^{238}U, and ^{239}Pu, and Antineutrino-Induced Reactions." *Physics Review C* 22 (1980).

Berger, B. "First Results from KamLAND." *Intersections of Particle and Nuclear Physics: 8th Conference*, 2003.

Bernstein, A. *Personal communication* (2007).

Bernstein, A. *Personal communication* (2006).

Bernstein, A., Y. Wang, G. Gratta, and T. West. "Nuclear Reactor Safeguards and Monitoring with Antineutrino Detectors." *Journal of Applied Physics* 91 (2002).

Constant, F. *Fundamental Laws of Physics.* Addison-Wesley Publishing Co., 1963.

Cowan, C, F. Reines, F. Harrison, E. Anderson, and F. Hayes. "Large Liquid Scintillation Detectors." *Physical Review*, 1953: 493-494.

Duderstadt, J., and L. Hamilton. *Nuclear Reactor Analysis.* John Wiley & Sons, 1976.

Eisenhower, D. "Atoms for Peace." *speech to the United Nations General Assembly.* December 8, 1953.

Fermi, E. "An Attempt at a Theory of β-Rays." *Zeitschrift fur Physik*, 1934: 161-177.

Fukuda, S., et al. "The Super-Kamiokande Detector." *Nuclear Instrumentation and Methods* A501 (2003).

Hermann, O., S. Bowman, M. Brady, and C. Parks. "Validation of the SCALE System for PWR Spent Fuel Isotopic Composition Analyses." *ORNL/TM-12667*, 1995.

Huber, P., and T. Schwetz. "Precision Spectroscopy with Reactor Anti-neutrinos." *Physics Review D* 60 (2004).

IAEA. *Model Protocol Additional to the Agreement(s) Between the State(s) and International Atomic Energy Agency for the Application of Safeguards.* INFCIRC/540, 1997.

IAEA. "Non-Proliferation of Nuclear Weapons and Nuclear Security." 2006.
—. "Statute of the International Atomic Energy Agency." 1957.

IAEA. *The Text of the Agreement of 2 October 1974 Between Ecuador and the Agency For the Application of Safeguards in Connection with the Treaty for the Prohibition of Nuclear Weapons in Latin America and the Treaty on the Non-Proliferation of Nuclear Weapons.* INFCIRC/231, 1974.

IAEA. *Treaty on the Non-Proliferation of Nuclear Weapons.* INFCIRC/140, 1970.
Klimov, Yu., V. Kopeikin, L. Mikaelyan, K. Ozerov, and V. Sinev. "Neutrino Method Remote Measurement of Reactor Power and Power Output." *Atomic Energy* 76, no. 2 (1994).

Kozlov, Yu., et al. "Antineutrino-Deuteron Experiment at the Krasnoyarsk Reactor." *Journal of Atomic Nuclei* 63, no. 6 (2000): 1016-1019.

Kozlowski, T., and T. Downar. *Pressurised Water Reactor MOX/UO2 Core Transient Benchmark.* Nuclear Energy Agency Organisation for Economic Co-operation and Development, 2006.

Modro, S., et al. "Multi-Application Small Light Water Reactor Final Report." *INEEL/EXT-04-01626*, 2003.

Neito, M., A. Hayes, W. Wilson, C. Teeter, and W. Stanboro. "Detection of Anti-Neutrinos for Nonproliferation." *Nuclear Science and Engineering* 149 (2005).

Nezrick, F., and F. Reines. "Fission-Antineutrino Interaction with Protons." *Physical Review* 142, no. 4 (1966): 852-869.

Reines, F. "The Neutrino: From Poltergeist to Particle." *Rev. of Modern Physics* 68, no. 2 (1996).

Reines, F., and C. Cowan. "Detection of the Free Neutrino." *Physical Review*, 1953.

Rodejohann, W. "A Parameterization for the Neutrino Mixing Matrix." *Physical Review D* 69 (2004).

SCE and SDG&E. *Final Safety Analysis Report: San Onofre Nuclear Generating Station Units 2 & 3.* Southern California Edison Company and San Diego Gas & Electric Company, 1978.

Schwetz, T. 2004. http://www.ph.tum.de/~schwetz/reactor-neutrino-data/.

Soldatov, A. *Unpublished results* (2008).

Appendices

A. Simulation Power History Data

This appendix contains the power history data used for the simulations in ORIGEN-ARP. The units used in the tables are megawatts per metric ton of fuel. The days listed in the tables are the day in the cycle on which the power step ends.

Table A.1: Power history data for LEU simulation

Assembly	Day 131	Day 262	Day 392
1	30.65	27.90	27.51
2	39.30	34.58	33.79
3	27.11	26.33	27.11
4	36.94	34.97	34.97
5	45.58	42.05	41.65
6	44.01	40.08	38.90
7	40.47	37.33	36.55
8	32.62	31.83	31.83
9	41.26	39.69	39.30
10	32.22	33.01	34.19
11	43.23	42.44	41.65
12	36.94	36.55	36.94
13	48.73	48.73	48.73
14	32.62	31.83	31.83
15	45.58	44.80	45.19
16	45.98	45.58	44.80
17	42.83	47.94	50.30
18	34.19	36.55	37.72
19	46.37	49.12	49.91
20	38.90	41.26	41.65
21	27.11	26.33	27.11
22	41.26	39.69	39.30
23	45.98	45.19	44.80
24	34.19	35.76	36.15
25	36.55	38.51	38.90
26	47.16	49.51	49.51
27	34.19	36.94	37.72
28	42.83	49.12	51.48
29	36.94	34.97	34.97
30	32.22	33.01	34.19
31	42.83	47.94	50.30
32	36.55	38.51	38.90
33	35.37	36.55	35.76
34	46.76	45.58	43.23
35	44.80	44.40	42.44
36	35.37	36.94	36.94
37	45.58	42.05	41.65
38	43.23	42.44	41.65
39	34.19	36.55	37.72
40	47.16	49.51	49.51
41	46.76	45.58	43.23

42	35.37	35.37	34.58
43	45.58	44.40	42.44
44	46.37	47.16	46.76
45	30.65	27.90	27.51
46	44.01	40.08	38.90
47	36.94	36.55	36.94
48	45.98	49.12	49.91
49	34.19	36.94	37.72
50	44.40	44.40	42.44
51	45.19	44.01	42.44
52	30.65	31.83	32.62
53	27.51	29.86	31.04
54	38.90	34.58	33.79
55	40.08	37.33	36.55
56	48.73	48.73	49.12
57	38.90	41.26	41.65
58	42.44	49.12	51.48
59	34.97	36.55	36.94
60	45.98	46.76	46.76
61	27.11	29.47	31.04
62	21.61	25.15	27.51

Table A.2: Power history for MOX simulation, part 1

Assembly	**Day 1**	**Day 2**	**Day 3**	**Day 4**	**Day 5**	**Day 35**	**Day 65**	**Day 95**	**Day 125**	**Day 155**
1	18.00	18.00	17.00	17.00	18.00	17.37	16.90	17.00	17.27	17.63
2	21.00	21.00	20.00	21.00	20.00	20.47	19.97	20.00	20.33	20.73
3	26.00	25.00	25.00	25.00	25.00	24.93	24.13	24.17	24.47	24.97
4	22.00	21.00	21.00	21.00	20.00	20.80	20.20	20.23	20.57	21.03
5	15.00	13.00	14.00	14.00	14.00	13.70	13.67	13.93	14.33	14.73
6	29.00	28.00	28.00	28.00	27.00	27.93	27.57	27.80	28.23	28.77
7	43.00	43.00	43.00	42.00	43.00	42.63	41.33	41.13	41.33	41.67
8	48.00	48.00	49.00	48.00	48.00	48.00	47.63	48.10	48.77	49.40
9	47.00	48.00	47.00	47.00	47.00	46.87	45.20	44.77	44.90	45.23
10	48.00	49.00	48.00	48.00	48.00	48.07	47.57	47.97	48.63	49.40
11	15.00	13.00	14.00	14.00	14.00	13.70	13.67	13.93	14.33	14.73
12	36.00	36.00	36.00	35.00	36.00	35.73	35.60	36.07	36.77	37.40
13	49.00	49.00	49.00	49.00	49.00	48.93	49.90	51.20	52.33	53.27
14	52.00	51.00	51.00	51.00	51.00	51.00	50.33	50.17	50.10	50.07
15	51.00	51.00	50.00	51.00	50.00	50.53	49.87	49.63	49.53	49.50
16	43.00	42.00	42.00	41.00	42.00	41.77	40.90	40.53	40.37	40.27
17	48.00	47.00	47.00	48.00	47.00	47.23	46.60	46.30	46.27	46.33
18	29.00	28.00	28.00	28.00	27.00	27.93	27.57	27.80	28.23	28.77
19	49.00	49.00	49.00	49.00	49.00	48.93	49.90	51.20	52.33	53.27
20	41.00	41.00	40.00	40.00	41.00	40.27	40.83	41.33	41.73	41.97
21	56.00	56.00	56.00	56.00	56.00	56.13	58.17	59.47	60.07	60.27
22	53.00	52.00	52.00	53.00	52.00	52.27	52.37	52.03	51.60	51.03
23	56.00	56.00	57.00	56.00	57.00	56.47	58.10	58.83	58.93	58.80
24	45.00	43.00	44.00	43.00	44.00	43.63	43.77	43.50	43.13	42.80
25	18.00	18.00	17.00	17.00	18.00	17.37	16.90	17.00	17.27	17.63
26	43.00	43.00	43.00	42.00	43.00	42.63	41.33	41.13	41.33	41.67
27	52.00	51.00	51.00	51.00	51.00	51.00	50.33	50.17	50.10	50.07
28	56.00	56.00	56.00	56.00	56.00	56.13	58.17	59.47	60.07	60.27

29	46.00	45.00	45.00	45.00	45.00	45.30	46.27	46.57	46.43	46.10
30	58.00	57.00	58.00	58.00	58.00	58.10	60.37	61.10	61.10	60.67
31	51.00	51.00	50.00	51.00	51.00	50.87	51.33	50.90	50.23	49.50
32	59.00	59.00	59.00	59.00	60.00	59.33	60.93	61.10	60.73	60.13
33	21.00	21.00	20.00	21.00	20.00	20.47	19.97	20.00	20.33	20.73
34	48.00	48.00	49.00	48.00	48.00	48.00	47.63	48.10	48.77	49.40
35	51.00	51.00	50.00	51.00	50.00	50.53	49.87	49.63	49.53	49.50
36	53.00	52.00	52.00	53.00	52.00	52.27	52.37	52.03	51.60	51.03
37	58.00	57.00	58.00	58.00	58.00	58.10	60.37	61.10	61.10	60.67
38	51.00	50.00	51.00	50.00	50.00	50.47	50.27	49.37	48.37	47.47
39	47.00	46.00	46.00	46.00	46.00	46.17	45.60	44.37	43.27	42.33
40	52.00	51.00	51.00	52.00	51.00	51.30	50.73	49.37	48.07	46.97
41	26.00	25.00	25.00	25.00	25.00	24.93	24.13	24.17	24.47	24.97
42	47.00	48.00	47.00	47.00	47.00	46.87	45.20	44.77	44.90	45.23
43	43.00	42.00	42.00	41.00	42.00	41.77	40.90	40.53	40.37	40.27
44	56.00	56.00	57.00	56.00	57.00	56.47	58.10	58.83	58.93	58.80
45	51.00	51.00	50.00	51.00	51.00	50.87	51.33	50.90	50.23	49.50
46	47.00	46.00	46.00	46.00	46.00	46.17	45.60	44.37	43.27	42.33
47	55.00	54.00	54.00	54.00	54.00	54.13	53.47	51.87	50.33	49.10
48	59.00	59.00	60.00	59.00	60.00	59.63	60.97	60.50	59.57	58.57
49	22.00	21.00	21.00	21.00	20.00	20.80	20.20	20.23	20.57	21.03
50	48.00	49.00	48.00	48.00	48.00	48.07	47.57	47.97	48.63	49.40
51	48.00	47.00	47.00	48.00	47.00	47.23	46.60	46.30	46.27	46.33
52	45.00	43.00	44.00	43.00	44.00	43.63	43.77	43.50	43.13	42.80
53	59.00	59.00	59.00	59.00	60.00	59.33	60.93	61.10	60.73	60.13
54	52.00	51.00	51.00	52.00	51.00	51.30	50.73	49.37	48.07	46.97
55	59.00	59.00	60.00	59.00	60.00	59.63	60.97	60.50	59.57	58.57
56	48.00	47.00	47.00	48.00	47.00	47.27	47.47	46.40	45.23	44.30

Table A.3: Power history data for MOX simulation, part 2

Assembly	**Day 185**	**Day 215**	**Day 245**	**Day 275**	**Day 305**	**Day 335**	**Day 365**	**Day 395**	**Day 425**	**Day 455**
1	18.10	18.53	19.03	19.53	20.00	20.47	20.97	21.40	21.90	22.33
2	21.20	21.70	22.17	22.63	23.10	23.53	24.00	24.40	24.77	25.13
3	25.60	26.17	26.83	27.47	28.10	28.70	29.23	29.80	30.27	30.70
4	21.60	22.20	22.80	23.40	24.00	24.60	25.10	25.63	26.13	26.57
5	15.17	15.63	16.03	16.47	16.93	17.33	17.77	18.20	18.60	19.07
6	29.27	29.80	30.27	30.77	31.20	31.67	32.07	32.47	32.87	33.23
7	42.10	42.50	42.93	43.37	43.77	44.13	44.50	44.83	45.17	45.43
8	50.10	50.67	51.13	51.60	51.93	52.17	52.40	52.50	52.57	52.53
9	45.70	46.20	46.73	47.23	47.73	48.20	48.60	48.97	49.23	49.47
10	50.17	50.90	51.57	52.13	52.60	53.03	53.33	53.57	53.70	53.73
11	15.17	15.63	16.03	16.47	16.93	17.33	17.77	18.20	18.60	19.07
12	38.07	38.63	39.17	39.70	40.17	40.60	41.07	41.47	41.83	42.27
13	53.97	54.50	54.90	55.13	55.37	55.40	55.47	55.40	55.33	55.27
14	50.00	49.90	49.77	49.63	49.50	49.30	49.10	48.90	48.70	48.50
15	49.47	49.40	49.37	49.27	49.20	49.07	48.93	48.83	48.67	48.50
16	40.30	40.33	40.40	40.47	40.50	40.60	40.63	40.67	40.73	40.73
17	46.40	46.50	46.67	46.73	46.83	46.90	46.97	46.97	46.97	46.97
18	29.27	29.80	30.27	30.77	31.20	31.67	32.07	32.47	32.87	33.23
19	53.97	54.50	54.90	55.13	55.37	55.40	55.47	55.40	55.33	55.27

20	42.10	42.23	42.23	42.20	42.20	42.13	42.10	42.03	42.00	41.97
21	60.20	59.90	59.50	59.03	58.53	58.00	57.43	56.90	56.37	55.90
22	50.50	49.90	49.37	48.83	48.33	47.83	47.43	47.03	46.67	46.33
23	58.47	58.03	57.63	57.13	56.63	56.17	55.67	55.20	54.80	54.33
24	42.43	42.17	41.90	41.63	41.47	41.27	41.10	40.97	40.90	40.77
25	18.10	18.53	19.03	19.53	20.00	20.47	20.97	21.40	21.90	22.33
26	42.10	42.50	42.93	43.37	43.77	44.13	44.50	44.83	45.17	45.43
27	50.00	49.90	49.77	49.63	49.50	49.30	49.10	48.90	48.70	48.50
28	60.20	59.90	59.50	59.03	58.53	58.00	57.43	56.90	56.37	55.90
29	45.67	45.23	44.73	44.30	43.90	43.50	43.13	42.83	42.57	42.33
30	60.03	59.30	58.57	57.83	57.10	56.40	55.73	55.10	54.57	54.07
31	48.77	48.13	47.50	46.97	46.47	46.00	45.63	45.27	45.00	44.77
32	59.43	58.73	58.07	57.43	56.80	56.20	55.70	55.20	54.77	54.33
33	21.20	21.70	22.17	22.63	23.10	23.53	24.00	24.40	24.77	25.13
34	50.10	50.67	51.13	51.60	51.93	52.17	52.40	52.50	52.57	52.53
35	49.47	49.40	49.37	49.27	49.20	49.07	48.93	48.83	48.67	48.50
36	50.50	49.90	49.37	48.83	48.33	47.83	47.43	47.03	46.67	46.33
37	60.03	59.30	58.57	57.83	57.10	56.40	55.73	55.10	54.57	54.07
38	46.60	45.90	45.27	44.77	44.30	43.90	43.63	43.37	43.17	43.03
39	41.57	41.00	40.50	40.17	39.90	39.73	39.57	39.53	39.50	39.53
40	46.07	45.30	44.77	44.27	43.90	43.63	43.40	43.27	43.13	43.10
41	25.60	26.17	26.83	27.47	28.10	28.70	29.23	29.80	30.27	30.70
42	45.70	46.20	46.73	47.23	47.73	48.20	48.60	48.97	49.23	49.47
43	40.30	40.33	40.40	40.47	40.50	40.60	40.63	40.67	40.73	40.73
44	58.47	58.03	57.63	57.13	56.63	56.17	55.67	55.20	54.80	54.33
45	48.77	48.13	47.50	46.97	46.47	46.00	45.63	45.27	45.00	44.77
46	41.57	41.00	40.50	40.17	39.90	39.73	39.57	39.53	39.50	39.53
47	48.07	47.27	46.67	46.17	45.77	45.50	45.30	45.13	45.03	45.00
48	57.60	56.87	56.20	55.60	55.13	54.73	54.40	54.10	53.83	53.67
49	21.60	22.20	22.80	23.40	24.00	24.60	25.10	25.63	26.13	26.57
50	50.17	50.90	51.57	52.13	52.60	53.03	53.33	53.57	53.70	53.73
51	46.40	46.50	46.67	46.73	46.83	46.90	46.97	46.97	46.97	46.97
52	42.43	42.17	41.90	41.63	41.47	41.27	41.10	40.97	40.90	40.77
53	59.43	58.73	58.07	57.43	56.80	56.20	55.70	55.20	54.77	54.33
54	46.07	45.30	44.77	44.27	43.90	43.63	43.40	43.27	43.13	43.10
55	57.60	56.87	56.20	55.60	55.13	54.73	54.40	54.10	53.83	53.67
56	43.43	42.83	42.33	42.00	41.70	41.50	41.40	41.33	41.33	41.37

Table A.4: Power history data for MASLWR simulation

Day	Assembly 1	Assembly 2	Assembly 3
16.75	33.42	33.21	28.91
33.48	33.24	33.15	29.06
50.35	33.03	33.06	29.25
67.32	32.81	33.00	29.43
84.50	32.57	32.91	29.64
101.78	32.33	32.81	29.89
119.31	32.05	32.72	30.13
136.89	31.81	32.63	30.37
154.73	31.53	32.54	30.59
172.58	31.29	32.48	30.83

190.44	31.08	32.39	31.01
208.41	30.86	32.33	31.20
226.09	30.71	32.26	31.35
243.60	30.59	32.23	31.44
260.95	30.50	32.20	31.50
278.10	30.44	32.17	31.53
294.95	30.40	32.17	31.53
311.56	30.40	32.17	31.53
328.14	30.40	32.17	31.47
344.40	30.44	32.20	31.41
360.67	30.47	32.23	31.35
376.52	30.53	32.26	31.29
392.35	30.59	32.30	31.20
407.74	30.68	32.33	31.08
423.49	30.74	32.36	30.98
439.24	30.80	32.42	30.89
454.51	30.89	32.45	30.77
469.73	30.98	32.51	30.68
484.91	31.08	32.54	30.56
500.05	31.17	32.57	30.47
515.16	31.26	32.63	30.34
530.21	31.35	32.66	30.22
545.23	31.44	32.72	30.13
560.24	31.53	32.75	30.01
574.63	31.65	32.81	29.89
589.51	31.75	32.84	29.76
604.40	31.84	32.91	29.67
618.65	31.96	32.94	29.55
632.85	32.08	33.00	29.43
647.62	32.17	33.03	29.31
661.73	32.30	33.09	29.18
675.81	32.42	33.15	29.06
689.84	32.54	33.18	28.94
703.83	32.66	33.24	28.82
717.77	32.78	33.30	28.67
731.00	32.94	33.33	28.54
744.88	33.06	33.39	28.42
758.68	33.18	33.45	28.27
771.77	33.33	33.48	28.15
785.52	33.45	33.55	28.03
798.53	33.61	33.58	27.87
812.19	33.73	33.64	27.75
825.09	33.88	33.67	27.63
838.69	34.00	33.73	27.51
851.48	34.16	33.76	27.39
865.02	34.28	33.82	27.23

877.75	34.43	33.85	27.11
891.20	34.55	33.88	26.99
903.86	34.70	33.94	26.87
916.46	34.86	33.97	26.75
929.81	34.98	34.00	26.62
942.34	35.13	34.03	26.50
954.82	35.28	34.06	26.38
968.08	35.41	34.09	26.26
980.50	35.56	34.13	26.14
993.71	35.68	34.16	26.01
1006.03	35.83	34.16	25.89
1019.16	35.95	34.19	25.80
1031.42	36.11	34.22	25.68
1044.51	36.23	34.25	25.56
1056.68	36.38	34.25	25.46
1069.72	36.50	34.25	25.34
1082.70	36.63	34.28	25.25
1095.68	36.75	34.28	25.16
1108.63	36.87	34.31	25.04
1121.55	36.99	34.31	24.98
1134.43	37.11	34.31	24.88
1147.28	37.24	34.31	24.79
1160.08	37.36	34.31	24.70
1173.83	37.45	34.28	24.64
1186.57	37.57	34.28	24.58
1200.26	37.66	34.25	24.52
1213.90	37.75	34.25	24.46
1228.53	37.82	34.22	24.43
1242.13	37.91	34.22	24.37
1256.70	37.97	34.19	24.34
1272.27	38.00	34.16	24.34
1286.81	38.06	34.13	24.31
1302.37	38.09	34.09	24.27
1317.91	38.12	34.09	24.27
1334.49	38.12	34.06	24.27
1351.10	38.12	34.03	24.31
1368.77	38.09	34.00	24.31
1386.47	38.06	33.97	24.34
1403.08	38.06	33.97	24.34

B. Assembly Properties

This appendix lists the physical properties of the fuel assemblies modeled in the simulations. The data was taken from *Nuclear Reactor Analysis*. (Duderstadt and Hamilton 1976)

Table B.1: Properties of fuel assemblies used in simulations

	Westinghouse (LEU, MOX, MASLWR)	**Westinghouse CE (SONGS)**
Fuel Array	17x17	16x16
Rod Pitch (cm)	1.25	1.28
Rod O.D. (cm)	0.94	0.97
Clad Thickness (cm)	0.0572	0.0635
Fuel Pellet diameter (cm)	0.819	0.825
Pellet-Clad Gap (cm)	0.0082	0.0089